The PSZ-MCMF catalogue of *Planck* clusters over the DES region

D. Hernández-Lang [1,2]★ M. Klein,[1]★ J. J. Mohr,[1,3] S. Grandis [1] J.-B. Melin,[4] P. Tarrío,[4,5,6]
M. Arnaud,[5] G. W. Pratt,[4,5] T. M. C. Abbott,[7] M. Aguena,[8] O. Alves,[9] F. Andrade-Oliveira,[9] D. Bacon,[10]
E. Bertin,[11,12] D. Brooks,[13] D. L. Burke,[14,15] A. Carnero Rosell,[8,16,17] M. Carrasco Kind,[18,19] J. Carretero,[20]
F. J. Castander,[21,22] M. Costanzi,[23,24,25] L. N. da Costa,[8] M. E. S. Pereira,[26] S. Desai,[27] H. T. Diehl,[28]
P. Doel,[13] S. Everett,[29] I. Ferrero,[30] B. Flaugher,[28] J. Frieman,[28,31] J. García-Bellido,[32] D. Gruen,[2]
R. A. Gruendl,[18,19] J. Gschwend,[8,33] G. Gutierrez,[28] S. R. Hinton,[34] D. L. Hollowood,[35] K. Honscheid,[36,37]
D. J. James,[38] K. Kuehn,[39,40] N. Kuropatkin,[28] O. Lahav,[13] C. Lidman,[41,42] P. Melchior,[43]
J. Mena-Fernández,[44] F. Menanteau,[18,19] R. Miquel,[45,20] A. Palmese,[46] F. Paz-Chinchón,[18,47] A. Pieres,[8,33]
A. A. Plazas Malagón,[43] M. Raveri,[48] M. Rodriguez-Monroy,[44] A. K. Romer,[49] V. Scarpine,[28]
I. Sevilla-Noarbe,[44] M. Smith,[50] E. Suchyta,[51] G. Tarle,[9] D. Thomas,[10] N. Weaverdyck[9,52]
and (DES Collaboration)

Affiliations are listed at the end of the paper

ABSTRACT

We present the first systematic follow-up of *Planck* Sunyaev–Zeldovich effect (SZE) selected candidates down to signal-to-noise (S/N) of 3 over the 5000 deg^2 covered by the Dark Energy Survey. Using the MCMF cluster confirmation algorithm, we identify optical counterparts, determine photometric redshifts, and richnesses and assign a parameter, f_{cont}, that reflects the probability that each SZE-optical pairing represents a random superposition of physically unassociated systems rather than a real cluster. The new PSZ-MCMF cluster catalogue consists of 853 MCMF confirmed clusters and has a purity of 90 per cent. We present the properties of subsamples of the PSZ-MCMF catalogue that have purities ranging from 90 per cent to 97.5 per cent, depending on the adopted f_{cont} threshold. Halo mass estimates M_{500}, redshifts, richnesses, and optical centres are presented for all PSZ-MCMF clusters. The PSZ-MCMF catalogue adds 589 previously unknown *Planck* identified clusters over the DES footprint and provides redshifts for an additional 50 previously published *Planck*-selected clusters with S/N>4.5. Using the subsample with spectroscopic redshifts, we demonstrate excellent cluster photo-z performance with an RMS scatter in $\Delta z/(1 + z)$ of 0.47 per cent. Our MCMF based analysis allows us to infer the contamination fraction of the initial S/N>3 *Planck*-selected candidate list, which is ∼50 per cent. We present a method of estimating the completeness of the PSZ-MCMF cluster sample. In comparison to the previously published *Planck* cluster catalogues, this new S/N>3 MCMF confirmed cluster catalogue populates the lower mass regime at all redshifts and includes clusters up to z∼1.3.

Key words: galaxies: clusters: general – galaxies: clusters: intracluster medium – galaxies: distances and redshifts.

1 INTRODUCTION

The intracluster medium (ICM) in galaxy clusters can be detected through what are now easily observed ICM signatures, providing a means to select cluster samples based on their ICM properties. At high temperatures of up to $T \sim 10^8$ K (for massive clusters), photons are emitted at X–ray wavelengths via thermal Bremsstrahlung. Moreover, the ICM can leave an imprint on the cosmic microwave background (CMB). At mm-wavelengths, it is possible to study galaxy clusters via the thermal Sunyaev–Zeldovich effect (SZE; Sunyaev & Zeldovich 1972), which is produced by inverse Compton scattering of CMB photons by hot electrons in the ICM.

Large X–ray selected galaxy cluster catalogues have been created using X-ray imaging data from the *ROSAT All Sky Survey* and the *XMM-Newton* telescope (e.g. Piffaretti et al. 2011; Klein et al. 2019; Finoguenov et al. 2020; Koulouridis et al. 2021) as well as the recently launched eROSITA mission (Brunner et al. 2022; Klein et al. 2022; Liu et al. 2022). The *Planck* mission mapped the whole sky between 2009 and 2013 in mm and infrared wavelengths, with the goal of studying CMB anisotropies. The latest cluster catalogue released by the *Planck* collaboration is the second *Planck* catalogue of Sunyaev–Zeldovich sources (PSZ2; Planck Collaboration 2016), containing over 1600 cluster candidates down to a signal-to-noise ratio (S/N) of 4.5, detected from the 29-month full-mission data. Other projects such as the *South Pole Telescope* (*SPT*; Carlstrom

★ E-mail: daniel.hernandez@physik.lmu.de (DHL);
Matthias.Klein@physik.uni-muenchen.de (MK)

et al. 2011) and the *Atacama Cosmology Telescope* (*ACT*; Marriage et al. 2011) have also been used to create large SZE selected cluster catalogues (e.g. Bleem et al. 2015, 2020; Hilton et al. 2021).

Although ICM-based cluster selection from an X-ray or SZE sky survey is efficient, the resulting candidate lists must be optically confirmed to extract galaxy based observables such as precise photometric redshifts (e.g. Staniszewski et al. 2009; High et al. 2010; Song et al. 2012b; Liu et al. 2015; Klein et al. 2019, 2022). The optical followup also allows for a cleaning or removal of the contaminants (falsely identified clusters) from ICM selected samples, because noise fluctuations in the ICM candidate lists do not have physically associated galaxy systems. It is possible for a noise fluctuation in the ICM candidate list to overlap by chance with a physically unassociated galaxy system. With the use of the Multi-Component Matched Filter followup technique (MCMF; Klein et al. 2018, 2019), it is possible to account for this random superposition possibility for each ICM cluster candidate and to deliver empirically estimated, precise, and accurate measurements of the residual contamination in the final cluster catalogue.

To enable efficient optical followup and precise estimates of the purity of the final confirmed cluster catalogue, large, and homogeneous photometric data sets are beneficial. The Dark Energy Survey (DES; Abbott et al. 2016) covers ~5000 deg^2 with deep, multiband imaging in *g*-, *r*-, *i*-, *z*-, *Y*-bands with the DECam instrument (Flaugher et al. 2015). These imaging data are processed and calibrated using the DES data management system (Morganson et al. 2018), and to date two major data releases have taken place (Abbott et al. 2018, 2021).

Large, homogeneous multiband imaging surveys also support the direct galaxy-based selection of cluster catalogues (e.g. Gladders et al. 2007; Rykoff et al. 2014; Maturi et al. 2019; Wen & Han 2022). However, without a second cluster observable, as in the case of the ICM based selection followed up by optical confirmation, it is more challenging to empirically estimate or control the contamination of the final cluster catalogue. One can use statistical comparisons to well understood ICM-based samples (see SPT×RM analyses in Grandis et al. 2020, 2021) to estimate the contamination (as well as the mass completeness modeling) or one can attempt to simulate the contamination of the cluster sample directly (e.g. Song et al. 2012a; Crocce et al. 2015; DeRose et al. 2019), in which case the contamination estimates are impacted by the level of realism of the simulations.

The utility of optically based cluster sample cleaning methods, like that available with the MCMF algorithm, becomes ever more central to the cluster catalogue creation as one considers lower signal-to-noise ICM signatures as cluster candidates, because these candidate samples are more contaminated with noise fluctuations. With an effective optically based cleaning method, it becomes possible to create dramatically larger confirmed cluster samples from a given X-ray or mm-wave survey, while still maintaining low levels of contamination (i.e. high sample purity). As an example, the X-ray cluster sample MARDY3 selected from ROSAT in combination with DES produced an increase of an order of magnitude in the number of ROSAT selected clusters over the DES area (Klein et al. 2019). Significant gains are currently being seen in the extraction of cluster samples from lower signal-to-noise candidate lists from the SPT-SZ 2500d and the SPTpol 500-d survey (Klein et al., in preparation; Bleem et al., in preparation).

Leveraging the rich data set provided by *Planck*, we have developed a new cluster candidate catalogue that extends to lower signal-to-noise levels (S/N>3), enhancing the number of candidate

clusters identified. However, extending the catalogue to lower signal-to-noise levels leads to a higher number of spurious sources or noise fluctuations being classified as *Planck* detections, resulting in a decrease in the candidate catalogue purity. To address this reduced purity, we utilize the DES data set together with the MCMF cluster confirmation algorithm to confirm *Planck* clusters and to reject spurious sources.

In this analysis, we present the PSZ-MCMF[1] cluster catalogue. To construct this catalogue, we extend the MCMF tool to deal with the larger positional uncertainties that come with *Planck*-selected cluster candidates and then apply this tool to a *Planck*-based candidate list down to S/N = 3 using DES photometric data. In Section 2 we give a description of the DES and *Planck* data used. In Section 3 we describe the enhanced MCMF cluster confirmation method, while in Section 4 we report our findings. Finally, in Section 5 we summarize our findings and report our conclusions. Throughout this paper we adopt a flat Λ cold dark matter cosmology with $\Omega_M = 0.3$ and $H_0 = 70 \; \mathrm{km \, s^{-1} \, Mpc^{-1}}$.

2 DATA

2.1 DES multiband photometric data

In this work we use the DES Y3A2 GOLD photometric data, which is based on DES imaging data obtained from the first 3 yr of the survey (Abbott et al. 2018). We employ *g*-, *r*-, *i*-, *z*-band photometry, which has 95 per cent completeness limits of 23.72, 23.34, 22.78, and 22.25 mag, respectively. The YA32 GOLD catalogue has been optimized for cosmological studies with DES, similar to the Y1A1 GOLD catalogue (Drlica-Wagner et al. 2018). Because we build upon the same MCMF cluster confirmation method applied in a ROSAT×DES analysis (Klein et al. 2019), we refer the reader to that source for further details of the filtering and handling of the optical multiband data.

In summary, we make use of the single-object fitting photometry, which is based on the ngmix code (Sheldon 2014). The photometry is performed by fitting a galaxy model for each source in each single epoch image of a given band at the same time, interpolating the point spread functions at the location of each source. This fitting is done masking neighbouring sources. We make use of the star-galaxy separator included in the GOLD catalogues (Drlica-Wagner et al. 2018) and exclude unresolved objects with *i* <22.2 mag. We also make use of the masking provided by Y3A2 GOLD (similar to that described in Y1A1 GOLD; Drlica-Wagner et al. 2018) to exclude regions around bright stars.

2.2 Planck SZE candidate list

We build a catalogue of *Planck* SZE sources with S/N>3 located within the DES footprint. The SZE catalogue is created using a matched multifilter (MMF) approach (see for example Herranz et al. 2002; Melin, Bartlett & Delabrouille 2006), namely the MMF3 algorithm used and described in Planck Collaboration (2014) and improved for the PSZ2 catalogue. The cluster detection is done using a combination of the *Planck* maps and assuming prior knowledge on the cluster profile. In this application of MMF3, we divide the sky into patches of 10° × 10°, generating 504 overlapping patches, and

---

[1]PSZ stands for the *Planck* Sunyaev–Zeldovich cluster candidate list, whereas MCMF comes from the algorithm, which allows us to maximize the number of clusters from any given parent candidate list.
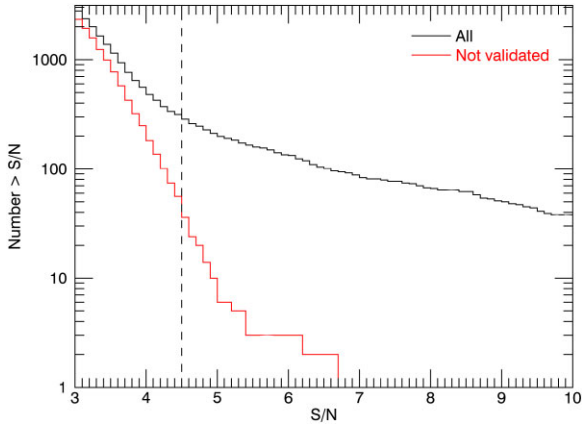
Figure 1. Cumulative number of *Planck* cluster candidates down to S/N = 3. The solid black line represents the full sample of 3130 candidates. The solid red line represents the 2670 candidates that have not been validated in previous works via a simple cross-identification with known SZE and X-ray clusters (see text). The dashed line corresponds to the S/N = 4.5 limit for the PSZ2 catalogue (Planck Collaboration 2016).

run the detection algorithm with two iterations; the first iteration detects the SZE signal and the second refines the SZE candidate position to allow for improved estimation of the S/N and other properties.

The filter works by combining the frequency maps from the *Planck* survey into a vector $M(x)$, where each component corresponds to a map at frequency ν_i with $i = 1, ..., N$ with N being the total number of maps. For *Planck*, we use the channel maps from 100 to 857 GHz, which correspond to the six highest-frequency maps.

For each cluster candidate at a given central position x_0, the algorithm fits,

$$M_\nu(x) = y_0 \, j_\nu \, T_{\theta_c}(x - x_0) + n_\nu(x), \tag{1}$$

where y_0 is the central value at position x_0 and $n_\nu(x)$ corresponds to the noise vector, which is the sum of the other emission components in the map that do not correspond to the cluster SZE (such as, e.g. primordial CMB anisotropies and diffuse galactic emission). The frequency dependence of the SZE is represented by j_ν. The spatial profile is defined as T_{θ_c}, with θ_c as the core radius. The assumed profile is chosen to be the universal pressure profile (Arnaud et al. 2010).

The filter is then employed to minimize the total variance estimate $\sigma_{\theta_c}^2$ on y_0 for each detected candidate, which yields an estimate $\hat{y}_0$. The S/N is then defined as $\hat{y}_0/\sigma_{\theta_c}$.

From this analysis we get the positions and associated uncertainties of the SZE sources plus the S/N and the SZE flux. At S/N>3, we get a total of 3130 *Planck* SZE sources (i.e. cluster candidates). Fig. 1 shows the cumulative number of cluster candidates (black) and unvalidated cluster candidates (red) for each S/N bin within the DES footprint. A candidate is considered to be validated if (1) it is less than 5 arcmin from a confirmed cluster (with known redshift) of the Meta-Catalog of SZ detected clusters (MCSZ) of the M2C database,[2] or (2) it is less than 10 arcmin and less than θ_{500} from a confirmed cluster in the Meta-Catalog of X-Ray Detected Clusters of Galaxies (MCXC; Piffaretti et al. 2011). From the full sample of 3130 candidates, 460 have been validated in this way (with 414 matching MCSZ clusters, and 46 matching MCXC only), while the
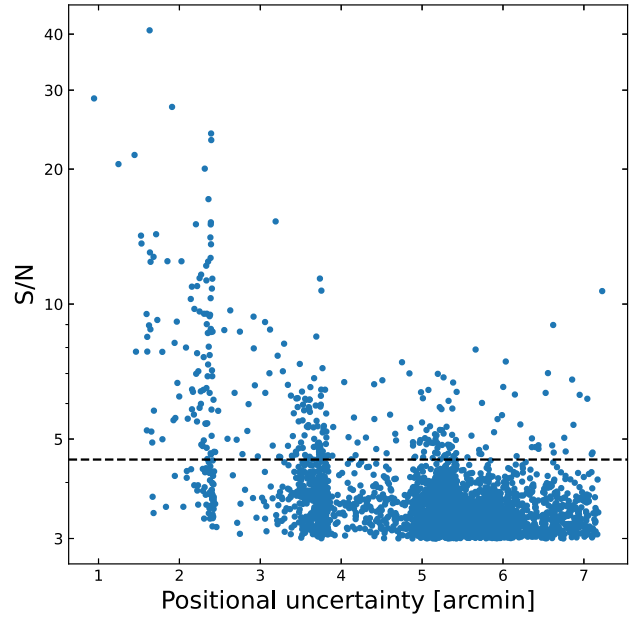
Figure 2. Positional uncertainty distribution in units of arcminutes versus *Planck* candidate S/N. The mean and median of the sources with S/N<4.5 are 5.26 and 5.36 arcmin, respectively. The black dashed line represents the threshold at S/N = 4.5.

remaining 2670 are non-validated candidates but may nevertheless be real galaxy clusters.

Fig. 2 contains the S/N versus the positional uncertainties of the *Planck* sources, where the black dashed line represents a S/N = 4.5. The apparent structure of the positional uncertainty is due to the pixelization of the *Planck* maps. The detection algorithm filters the maps and finds the pixel which maximizes the S/N. The position assigned for a detection corresponds to the pixel centre. The positional uncertainty is also computed on a pixelized grid.

We estimate the contamination of the *Planck* SZE candidate list using simulations. We use the *Planck* Sky Model (version 1.6.3; Delabrouille et al. 2013), to produce realistic all-sky mock observations. The simulations contain primary cosmic microwave background anisotropies, galactic components (synchrotron, thermal dust, free-free, spinning dust), extra-galactic radio and infrared point sources, and kinetic and thermal SZE. Each frequency map is convolved with the corresponding beam, and the instrumental noise consistent with the full mission is added. We run the thermal SZE detection algorithm down to S/N = 3, and we match the candidate list with the input cluster catalogue adopting a 5 arcmin matching radius. We perform the matching after removing regions of the sky with high dust emission, leaving 75 per cent of the sky available, and we only use input clusters with a measured Compton parameter Y in a circle of radius $5 \times R_{500},$[3] Y_{5R500}, above 2×10^{-4} arcmin². We adopt the SZE flux–mass relation,

$$E^{-2/3}(z) D_A^2(z) Y_{5R500} = A \left[\frac{M_{500}}{3 \times 10^{14} h_{70}^{-1} \, M_\odot}\right]^{5/3} \tag{2}$$

with $A = 2.59 \times 10^{-5} \, h_{70}^{-1}$ Mpc² (see equation B.3 in Arnaud et al. 2010). $E(z) = H(z)/H_0$ is the Hubble parameter normalized to

[3]R_{500} is defined as the radius within which the density is 500 times the critical density.
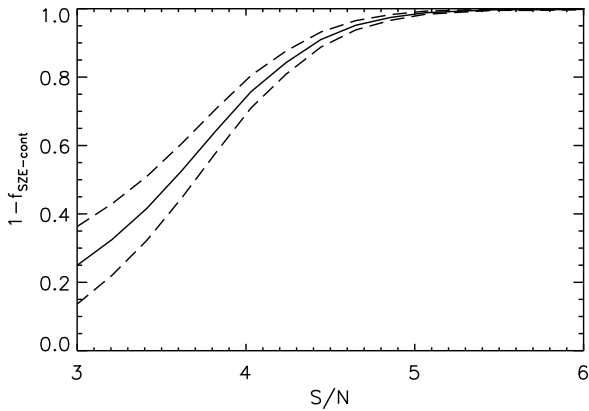
Figure 3. Purity as a function of signal-to-noise threshold of the cluster candidate list, estimated on *Planck* simulations. Dashed lines show the uncertainty of the estimated purity. The purity decreases from ∼1 at S/N>6 to ∼0.25 at S/N>3.

its present value and $D_A(z)$ is the angular diameter distance. The Compton parameter Y_{5R500} is given in steradians. We estimate the purity of the sample as the number of real clusters divided by the number of detected clusters. This ratio is computed for various S/N thresholds. The result is shown in Fig. 3. The uncertainty in purity is considered to be the difference between the best estimate and the lower limit of the purity (figs 11 and 12 in Planck Collaboration 2016, respectively) of the PSZ2 catalogue, for the union 65 per cent case. We fit this difference as a function of the contamination with a power law in the range S/N = 4.5-20. We extrapolate this down to S/N = 3. From here on, we refer to this contamination as the initial contamination: $f_{SZE\text{-}cont}$. At high S/N threshold (S/N>6), the purity, $1 - f_{SZE\text{-}cont}$, is close to unity. Reducing the S/N threshold to 4.5 leads to a purity close to 0.9, which is consistent with previous estimates (Planck Collaboration 2016). When reducing the threshold to S/N = 3, we measure a purity of ∼ 25 per cent corresponding to a contamination $f_{SZE\text{-}cont} = 0.75$ in the simulations.

3 CLUSTER CONFIRMATION METHOD

To identify optical counterparts and estimate photometric redshifts we use a modified version of the MCMF cluster confirmation algorithm on the *Planck* candidate list and DES-Y3 photometric catalogues. For each potential cluster, the radial position and the galaxy colour weightings are summed over all cluster galaxy candidates to estimate the excess number of galaxies, or richness (λ), with respect to the background. Klein et al. (2019) contains further details of MCMF weights and the counterpart identification method.

We expect only a fraction $1-f_{SZE\text{-}cont}$ of the *Planck* candidates to be real clusters, with a large fraction ($f_{SZE\text{-}cont} = 0.75$) corresponding to contaminants (we return to the value of $f_{SZE\text{-}cont}$ in Section 4.4.2). Most of these contaminants have no associated optical system, but some will happen to lie on the sky near a physically unassociated optical system or a projection of unassociated galaxies along the line of sight. We refer to these contaminants as 'random superpositions'. The MCMF method has been designed to enable us to remove these contaminants from the *Planck* candidate list. To estimate the likelihood of a 'random superposition' (e.g. a spurious *Planck* candidate being associated with one of the two cases above), we run MCMF at random positions in the portion of the sky survey that lies away from the candidates. With this information we can

reconstruct the frequency and redshift distribution of optical systems, and this allows us to estimate the probability that each candidate is a contaminant (see details in Section 3.2.2).

3.1 Cluster confirmation with MCMF

In the MCMF method the sky coordinates of the cluster candidates are used to search the multiband photometric catalogues with an associated galaxy red sequence (RS) model, to estimate galaxy richness λ as a function of redshift along the line of sight to each candidate. The weighted richnesses are estimated within a default aperture of R_{500} centreed at the candidate sky position (Klein et al. 2018, 2019). The weights include both a radial and a colour component, with the radial filter following a projected Navarro, Frenk, and White profile (NFW; Navarro, Frenk & White 1996, 1997), giving higher weights to galaxies closer to the centre. The colour filter uses the RS models and is tuned to give higher weights to cluster RS galaxies. These RS models are calibrated using over 2500 clusters and groups with spectroscopic redshifts from the literature, including: the SPT-SZ cluster catalogue (Bleem et al. 2015), the redMaPPer Y1 catalogue (only for clusters with spectroscopic redshifts; McClintock et al. 2019), and the 2RXS X-ray sources cross-matched with the MCXC cluster catalogue (Piffaretti et al. 2011). These richnesses are estimated for each redshift bin with steps of $\Delta z = 0.005$. The richness as a function of redshift is then searched to find richness peaks; the three strongest λ peaks, each with a different photometric redshift, are recorded for each candidate.

The mean positional uncertainty of the *Planck* sources is ∼5.3 arcmin, which, adopting the cosmology from Section 1, translates into an uncertainty of ∼0.6 Mpc and ∼1.9 Mpc at $z = 0.1$ and $z = 0.5$, respectively. Given the large positional uncertainty of the *Planck* candidates, the SZE position of a cluster could in some cases be offset by several times R_{500}. These large positional uncertainties enhance the probability of a spurious *Planck* candidate being paired to a physically unassociated optical system. To address this large positional uncertainty, we run the MCMF algorithm twice. The first run adopts the positions from the *Planck* candidate catalogue, and carries out a search for possible optical counterparts within an aperture that is three times the positional uncertainty of the candidate, corresponding to a mean aperture of ∼15.9 arcmin.

This first run gives us up to three possible optical counterparts for each *Planck* candidate, with the corresponding photometric redshift, optical centre, and λ for each. For all potential counterparts, the RS galaxy density maps are used to identify the peak richness, which is adopted as the optical centre. In the top row of Fig. 4 we show the richness distribution in redshift (estimated in this first run) of two different *Planck* candidates, at $z_{MCMF} \approx 0.24$ (left) and $z_{MCMF} \approx 0.88$ (right), with their corresponding pseudo-colour images shown on the bottom row.

All potential counterparts identified in the first run are then used for a second MCMF run with the goal of identifying the most likely optical counterpart for each *Planck* candidate and refining the estimation of the photometric redshift and richness. We proceed with the second run of MCMF using the optical counterpart positions as the input, but now using R_{500} as the aperture within which to search for counterparts. R_{500} is derived using a NFW profile and the *Planck* candidate mass estimation, M_{500}, at the redshift of each potential counterpart. For each candidate, redshift-dependant masses are estimated using the SZE mass proxy (for details see section 7.2.2 of Planck Collaboration 2014). The *Planck* flux measured with the matched filter is degenerate with the
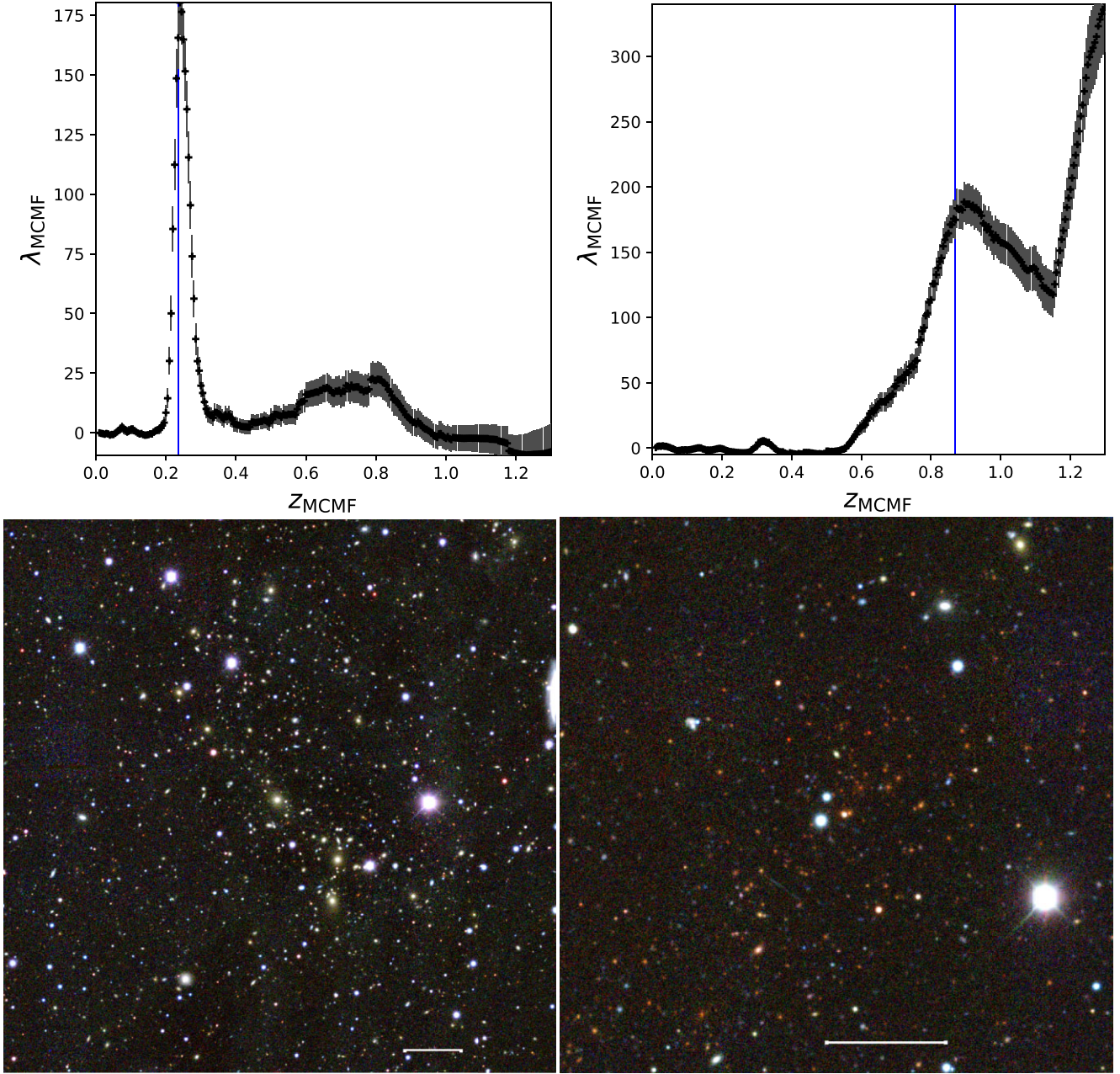
Figure 4. Example *Planck* cluster candidates with IDs PSZ-SN3 J2135 + 0124 ($z_{MCMF} = 0.24$, left) and PSZ-SN3 J0102-4915 ($z_{MCMF} = 0.87$, right). *Above:* Richness as a function of redshift for each candidate. The blue line marks the most likely redshift of the candidate. *Below:* DES pseudo-colour images at the cluster positions. The white bar at the bottom denotes a scale of 1 arcmin. North is up and east is to the left.

assumed size. We break this size-flux degeneracy using the flux–mass relation given by (see also equation 5 in Planck Collaboration 2014)

$$E^{-2/3}(z)\left[\frac{D_A^2(z)Y_{500}}{10^{-4}\text{Mpc}^2}\right] = 10^{-0.19}h_{70}^{-0.21}\left[\frac{M_{500}}{6\times10^{14}\,\text{M}_\odot}\right]^{1.79}, \quad (3)$$

where $E = H(z)/H_0$ and $H(z)$ is the Hubble parameter, and D_A is the angular diameter distance. This second run also gives us up to three redshift peaks for each source, but we select the richness peak whose redshift is the closest to the output redshift from the first run.

In summary, we obtain the positions and the redshifts of up to three potential optical counterparts with the first MCMF run, and in the second run we obtain the final redshifts and richnesses of each of these optical counterparts. The information from the second run allows us to select the most probable counterpart in most cases, with some candidates having more than one probable counterpart, as discussed below.

3.2 Quantifying probability of random superpositions

As already noted, with MCMF we leverage the richness distributions along random lines of sight in the survey as a basis for assigning a probability that each potential optical counterpart of a *Planck-*

selected candidate is a random superposition (e.g. it is not physically associated with the *Planck* candidate). We describe this process below.

3.2.1 Richness distributions from random lines of sight

A catalogue along random lines of sight is generated from the original *Planck* catalogue, where for each candidate position we generate a random position on the sky, with a minimum radius of approximately three times the mean positional uncertainty (5.5 arcmin). We also impose the condition that the random position has to be at least $\sim 3 \times 5.5$ arcmin away from any of the *Planck* candidates. We analyse the catalogue of random positions using MCMF in the same manner as for the data, except that, for the NFW profile used in the second run, the mass information needed to estimate the R_{500} is randomly selected from any of the *Planck* candidates (removing the candidate from which the random was generated).

To have sufficient statistics we select two random positions for each *Planck* candidate, so we have approximately two times as many random lines of sight as *Planck* candidates. Given the large positional uncertainties in the *Planck* candidate catalogue, optical counterparts of random lines of sight might be assigned to an optical counterpart of a *Planck* candidate. To account for this, we remove from our random lines of sight catalogue those positions that (1) have $\lambda \geq 30$ (e.g. lines of sight with massive clusters), and (2) are within 3 Mpc of any *Planck* source from our final, confirmed catalogue and have $|z_{\mathrm{Planck}} - z_{\mathrm{random}}| < 0.1$. Also, once the second set of random lines of sight has been analysed, we remove those positions that lie within 3 arcmin from any random source position from the first set to avoid double counting the same optical structures.

3.2.2 Estimating the random superposition probability f$_{cont}$

With the random lines of sight we can use the f_{cont} estimator presented in Klein et al. (2019), which is proportional to the probability of individual *Planck* candidates being random superpositions of physically unassociated structures (Klein et al. 2022). By imposing an f_{cont} threshold on our final cluster catalogue, we are able to quantify (and therefore also control) the contamination fraction. To estimate f_{cont} for each *Planck* candidate, we integrate the normalized richness distributions along random lines of sight $f_{\mathrm{rand}}(\lambda, z)$, within multiple redshift bins, that have $\lambda \geq \lambda_{\mathrm{src}}$, where λ_{src} is the richness of the *Planck* candidate. We do the same for the richness distribution of the *Planck* candidates $f_{\mathrm{obs}}(\lambda, z)$ and then we estimate f_{cont} as the ratio,

$$f_{\mathrm{cont}}(\lambda_{\mathrm{src}}, z) = \frac{\int_{\lambda_{\mathrm{src}}}^{\infty} \mathrm{d}\lambda \, f_{\mathrm{rand}}(\lambda, z)}{\int_{\lambda_{\mathrm{src}}}^{\infty} \mathrm{d}\lambda \, f_{\mathrm{obs}}(\lambda, z)}. \quad (4)$$

In Fig. 5 we show three examples of *Planck* candidates with the estimated f_{cont}. The blue and orange lines are the interpolated richness distributions of *Planck* candidates and of random lines of sight, respectively, at the redshift of the best optical counterpart. The orange (blue) shaded area shows the integral in the numerator (denominator) in equation (4), starting at the richness λ_{src} of the *Planck* candidate.

In simple terms, a constant value of f_{cont} can be translated to a redshift-varying richness value $\lambda(z)$. Thus, selecting candidates with a value of f_{cont} lower than some threshold, is similar to requiring the final cluster sample to have a minimum richness
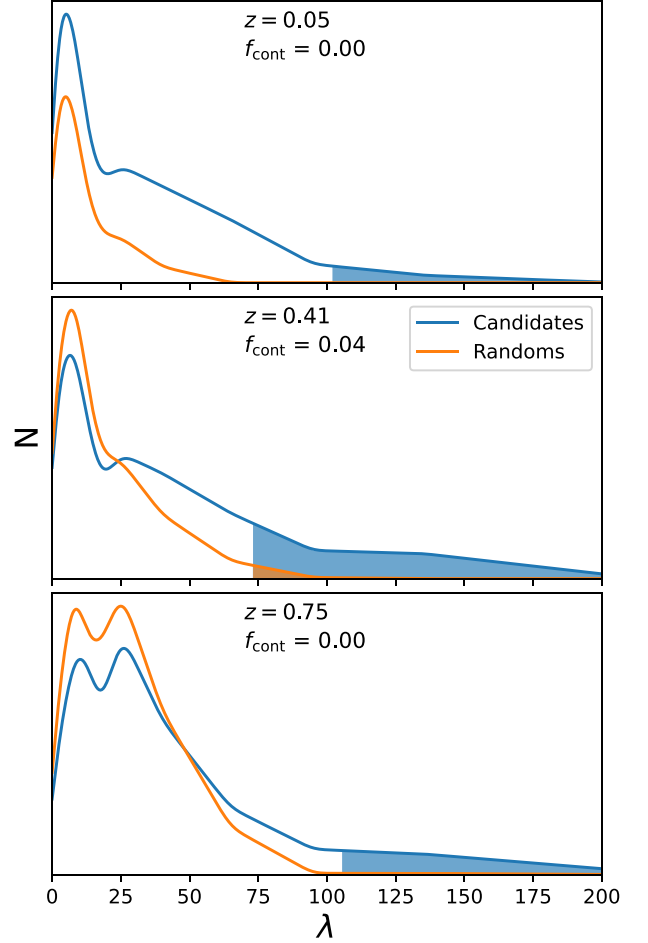

Figure 5. Examples of normalized richness distributions for random lines of sight (orange) and for *Planck* cluster candidates (blue) for all sources within an estimated $\delta z < 0.05$ of three *Planck* candidates shown from top to bottom at $z = 0.05, 0.41, 0.75$. For each of the sources, the area under the curves where the richness is equal to or greater than that of the *Planck* candidate is shaded. These shaded regions correspond to the numerator (orange) and denominator (blue) of equation (4).

that can vary with redshift [$\lambda_{\mathrm{min}}(z)$], above which the catalogue has a fixed level of contamination. We refer to this threshold as $f_{\mathrm{cont}}^{\mathrm{max}}$, which yields a catalogue contamination estimated as $f_{\mathrm{cont}}^{\mathrm{max}} \times$ (initial contamination), independent of redshift. Because the initial contamination of the *Planck*-selected sample is $f_{\mathrm{SZE\text{-}cont}}$ and the final contamination of the cluster sample selected to have $f_{\mathrm{SZE\text{-}cont}} < f_{\mathrm{cont}}^{\mathrm{max}}$ is $f_{\mathrm{cont}}^{\mathrm{max}} \times f_{\mathrm{SZE\text{-}cont}}$, one can think of the $f_{\mathrm{cont}}^{\mathrm{max}}$ selection threshold as the fraction of the contamination in the original candidate sample that ends up being included in the final confirmed cluster sample. Thus, through selecting an f_{cont} threshold one can control the level of contamination in the final confirmed cluster catalogue.

4 RESULTS

In Section 4.1 we present PSZ-MCMF, the confirmed cluster catalogue extracted from the *Planck* candidate list after an analysis of the DES optical followup information using the MCMF algorithm. We then discuss in more detail the mass estimates (Section 4.2), the cross-comparison with other ICM selected cluster catalogues
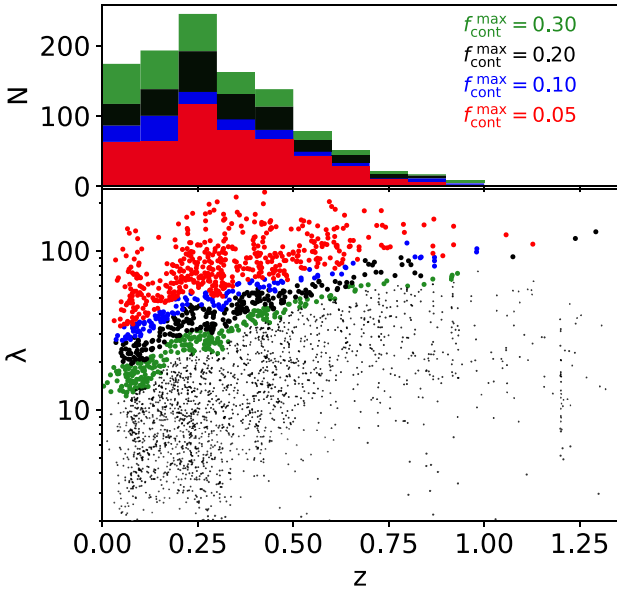
Figure 6. *Top:* Redshift distribution of the 2913 *Planck* candidates. The green, black, blue, and red histograms show the distributions of candidates with f_{cont} below $f_{cont}^{max} = 0.3, 0.2, 0.1$, and 0.05, respectively. *Bottom:* Richness versus redshift for the best optical counterpart for each *Planck* candidate. Pairs with a probability of being random superpositions (contamination) $f_{cont} > 0.3$ are shown as small black dots. Bigger green, black, blue, and red dots represent counterparts with $0.2 \leq f_{cont} < 0.3$, $0.1 \leq f_{cont} < 0.2$, $0.05 \leq f_{cont} < 0.1$, and $f_{cont} < 0.05$, respectively, corresponding to subsamples with decreasing contamination.

(Section 4.3), and the catalogue contamination and incompleteness (Section 4.4).

4.1 Creating the PSZ-MCMF cluster catalogue

As mentioned above, the MCMF algorithm allows us to identify up to three different richness peaks, corresponding to different possible optical counterparts, for each of the 3130 *Planck* candidates. To generate a final cluster catalogue, we select the most likely optical counterpart for each of the 3130 *Planck* candidates by choosing the counterpart that has the lowest probability f_{cont} of being a random superposition (i.e. of being a contaminant rather than a real cluster).

With MCMF we identify optical counterparts for 2938 of the 3130 *Planck* candidates, whereas for the remaining 192 *Planck* candidates no counterpart is found (see Section 4.1.2 for details). Of the 2938 candidates with optical counterparts, 2913 have unique counterparts, while the remaining 25 share their counterpart with another candidate that is closer to that counterpart (see Section 4.1.3 for details). Finally, we consider a candidate to be confirmed when its optical counterpart has f_{cont} below the threshold value $f_{cont}^{max} = 0.3$. This results in 1092 confirmed *Planck* clusters. Of these confirmed clusters, 120 have two prominent redshift peaks with f_{cont} below the threshold value f_{cont}^{max}, and are considered to be candidates with multiple optical counterparts.

The top panel of Fig. 6 shows the redshift distribution for different values of the threshold f_{cont}^{max}, while the bottom panel shows the richness as a function of the redshift for the best optical counterpart of the *Planck* candidates in this final catalogue. Small dots represent sources with an estimated $f_{cont} \geq 0.3$, while bigger dots are colour coded

Table 1. Number of confirmed *Planck* clusters with $f_{cont}^{max} = 0.3, 0.2, 0.1$ and 0.05 presented by row.

f_{cont}^{max}	S/N>3			S/N>4.5		
	N_{cl}	Purity	Comp.	N_{cl}	Purity	Comp.
0.3	1092	0.847	0.648	**264**	**0.974**	**0.990**
0.2	**842**	**0.898**	**0.530**	253	0.983	0.957
0.1	604	0.949	0.402	236	0.992	0.900
0.05	479	0.975	0.327	213	0.996	0.816

Results are split by S/N. The second and third columns, for each S/N subsample, show the purity of the sample (Section 4.4.1) and the completeness (Section 4.4.2). The PSZ-MCMF sample presented in this paper corresponds to clusters with more restrictive MCMF cleaning in the case of the low signal-to-noise sample than in the higher signal-to-noise sample. These subsamples (see discussion in Section 4.1.4) are listed in bold face.

as green, black, blue, or red according to whether $0.2 \leq f_{cont} < 0.3$, $0.1 \leq f_{cont} < 0.2$, $0.05 \leq f_{cont} < 0.1$, or $f_{cont} < 0.05$, respectively.

In Table 1 we show the number of cluster candidates with f_{cont} below different values of the threshold f_{cont}^{max}, and different *Planck* candidate S/N thresholds. With this analysis we are adding 589 (828) clusters to the *Planck* cluster sample at $f_{cont}^{max} = 0.2$ (0.3) when going from the *Planck* S/N>4.5 to S/N>3.

4.1.1 Candidates with a second optical counterpart

If the cluster candidate has two prominent redshift peaks with $f_{cont} < f_{cont}^{max} = 0.3$, where either (1) the redshift offset $[\delta z = (z_1 - z_2)/(1 + z_1)]$ is greater than 2 per cent or (2) the on-sky separation is greater than 10 arcmin, then we classify this candidate as a one with multiple optical systems, because a second optical counterpart with $f_{cont} < 0.3$ is an indication that the probability of being a chance superposition is lower than $f_{cont}^{max} \times f_{SZE-cont}$. We give the redshifts, sky-positions, richnesses, and other values for this second optical counterpart in the full cluster catalogue. In the case that both counterparts have the same f_{cont}, we select the one that is closer to the *Planck* candidate position. In Appendix A we discuss a specific example.

4.1.2 Candidates with no optical counterpart

Out of the 3130 *Planck* candidates, there are 192 for which the MCMF analysis delivers no optical counterpart – not even with a high f_{cont}. Most of these candidates (all but 26) are located near the edges of the DES footprint, suggesting that with more complete optical data many of these candidates could be associated with an optical counterpart. The 26 candidates that lie away from the DES survey edge show either a bright star or bright low-z galaxy near the *Planck* position or a lack of photometric information in one or more DES bands. Regions of the sky with these characteristics are masked by MCMF and this is the likely reason that no optical counterpart is identified for those candidates.

4.1.3 Candidates sharing the same optical counterpart

Given the rather generous search aperture used in the first run of MCMF, it is possible that some *Planck* candidates lying near one another on the sky share the same optical counterpart. There are 41 candidates at $f_{cont} < 0.3$ that share 20 optical counterparts. The criteria we use to identify these 41 candidates is similar to the one used above to identify candidates with more than one possible optical

counterpart. If the distance between the optical counterparts for the two *Planck* candidates is less than 10 arcmin and the redshift offset satisfies $|\delta z| \leq 0.02$, then we consider the two candidates to be sharing the same optical counterpart. In Appendix B we discuss a specific example.

To account for such cases, we add a column to our catalogue that refers to which *Planck* candidate is the most likely SZE counterpart by using the distance between the SZE and the optical centres. The *Planck* candidate with the smallest projected distance from the optical centre normalized by the positional uncertainty of the *Planck* candidate is considered to be the most likely SZE source.

4.1.4 Final PSZ-MCMF sample

With considerations of this last class we end up with 2913 *Planck* candidates, which are the closest to their respective optical counterparts. Table 1 contains the numbers of confirmed clusters, the purity (Section 4.4.1), and the completeness (Section 4.4.2) for different selection thresholds in f_{cont} and S/N. Given how the catalogue contamination of *Planck* candidates depends strongly on the S/N threshold (see Fig. 3), we decide to use two different values of f_{cont}^{max} for the low S/N (S/N>3) and high S/N (S/N>4.5) samples. The low S/N sample will be defined as clusters with S/N>3 that meet the $f_{cont}^{max} = 0.2$ threshold (second row of the S/N>3 sample in Table 1), whereas the high S/N sample will be defined as clusters with S/N>4.5 that meet the $f_{cont}^{max} = 0.3$ threshold (first row of the S/N>4.5 sample in Table 1). The combination of these two samples corresponds to the PSZ-MCMF cluster sample, with a total of 853 clusters.

As previously noted in Section 3.2.2, the contamination fraction of the confirmed cluster sample is $f_{cont}^{max} \times f_{SZE-cont}$ and depends on the f_{cont} selection threshold applied. The full PSZ-MCMF cluster catalogue will be made available online at the VizieR archive.[4] Table B1 contains a random subsample of the PSZ-MCMF catalogue with a subset of the columns.

In much of the discussion that follows we focus on the PSZ-MCMF cluster catalogue; however, we will define two subsamples that will be used in specific cases: the low S/N sample and the high S/N sample. The low S/N sample ($f_{cont}^{max} = 0.2$ and S/N>3), consists of 842 clusters with a ∼90 per cent purity and 53 per cent completeness. The high S/N sample ($f_{cont}^{max} = 0.3$ and S/N>4.5) consists of 264 clusters with a ∼97 per cent purity and 99 per cent completeness. Other sample selections could be made, and the basic properties of twelve samples are presented in Table 1.

4.1.5 Comparison with spectroscopic redshifts

Starting with the ∼2500 clusters and groups with spectroscopic redshifts used to calibrate the RS models of MCMF, we cross-match the cluster positions with the optical coordinates of each of our *Planck* candidates, selecting as matches those that lie within an angular distance of 3 arcmin. We choose to match with the optical counterpart positions, because they provide a more accurate sky position than the *Planck* SZE positions, which have a typical uncertainty of 5 arcmin. We use this cross-matched sample of clusters with spectroscopic redshifts to refine the red-sequence models of the MCMF algorithm (Klein et al. 2019).

We find 181 clusters in common with the PSZ-MCMF cluster catalogue, including a $z = 1.1$ cluster (SPT-CL J2106-5844). Of this

sample, 18 clusters have another MCMF richness peak with f_{cont} below the threshold value $f_{cont}^{max} = 0.2$. Of these 18 candidates, the primary richness peak (lowest f_{cont}) in 16 shows good agreement with the corresponding spectroscopic redshift z_{spec}, while for the remaining two the secondary peak lies at the z_{spec}. Of the full cross-matched sample, there are two sources that have no secondary peak and exhibit a large redshift offset in the primary richness peak. We discuss these two cases in Appendix C1.

To characterise the redshift offset, we fit a Gaussian to the distribution of $\Delta z = (z_{spec} - z_{MCMF})/(1 + z_{spec})$ of the 181 clusters, finding that the standard deviation is $\sigma = 0.00468$ (indicating a typical MCMF redshift uncertainty of 0.47 per cent), with a mean offset $\mu = -0.00005$ (indicating no MCMF redshift bias). This is consistent with the previously reported results from applications of the MCMF algorithm (Klein et al. 2019).

4.2 Estimating PSZ-MCMF cluster masses

Each *Planck* candidate comes with a function $M_{500}^{Pl}(Y_{500}, z)$ that allows an initial mass estimate using the redshift and the SZE signal Y_{500} of the candidate (see equation 3). Therefore, for each of the 853 PSZ-MCMF clusters, we use the final photometric redshift from our MCMF analysis to estimate a mass.

It is important to note that candidates with multiple optical counterparts may have a biased SZE signature Y_{500} due to contributions from both physical systems, which would impact the estimated M_{500}^{Pl}. However, because we do not have enough information to be able to separate the SZE emission coming for each component of the multiple counterparts, we adopt masses that are derived from the redshift of the first ranked richness peak. These masses are biased as discussed further below, and we therefore present a different mass estimate M_{500} in the final PSZ-MCMF catalogue (see the example Table B1).

We expect a mass shift between the PSZ-MCMF cluster sample and both *SPT* and MARD-Y3, that is largely due to the hydrostatic mass bias that has not been accounted for in the *Planck* estimated masses (see e.g. von der Linden et al. 2014; Hoekstra et al. 2015; Planck Collaboration 2020; Melin et al. 2021). In contrast, the *SPT* and MARD-Y3 masses are calibrated to weak lensing mass measurements (Bocquet et al. 2019), and should not be impacted by hydrostatic mass bias. We therefore apply a systematic bias correction to the *Planck* masses to bring all samples onto a common mass baseline represented by M_{500}.

To be able to compare our masses with different surveys accurately, we use cross-matched clusters and estimate the median mass ratio between the *SPT*/MARD-Y3 and the *Planck* mass estimates (see Section 4.3.2 for details), finding a median of $M_{500}^{Pl}/M_{500} \approx 0.8$. This value is in agreement with both weak lensing (von der Linden et al. 2014; Hoekstra et al. 2015) and CMB lensing (Planck Collaboration 2020) analyses of *Planck* clusters. Therefore, we correct the masses of the PSZ-MCMF clusters identified in our current analysis by this factor. Because the previously published PSZ2 catalogue has masses that are calculated in a manner similar to the M_{500}^{Pl} described above, we correct PSZ2 masses also using a correction of $(1 - b) = 0.8$. However, we note a further shift of $M_{500}^{Pl}/M_{500}^{PSZ2} \approx 0.95$ with respect to our corrected masses, and so we further correct the PSZ2 masses for the final comparison.

It should be noted that the mass bias of *Planck* clusters is still an ongoing topic. In summary, the masses we present in the following sections and the final cluster catalogue Table B1 are denoted as M_{500} and are rescaled to be consistent with results from a range of weak

lensing calibration analyses. These masses are larger than the *Planck* masses M_{500}^{Pl} by a factor $1/0.8 = 1.25$.

4.3 Comparison to other ICM selected cluster catalogues

To check how the PSZ-MCMF cluster sample compares to others, we select three cluster catalogues that have been selected using ICM signatures and that lie within the DES footprint: MARD-Y3 (Klein et al. 2019), SPT-2500d (Bocquet et al. 2019) along with SPT-ECS (Bleem et al. 2020) and PSZ2. MARD-Y3 is an X–ray selected cluster catalogue confirmed with DES Y3 photometric data, using the same tools as for the *Planck* analysis presented here. This MARD-Y3 catalogue has 2900 clusters with $f_{cont} < 0.2$. On the other hand, both the *SPT* and PSZ2 cluster catalogues are based on SZE selection. For *SPT* we select sources with a redshift measurement (photometric or spectroscopic), giving a total of 964 clusters. It is worth noting that PSZ2 is an all sky survey, and for the comparison we select sources that lie within the DES survey region and have a redshift measurement (226 clusters).

4.3.1 Comparison to PSZ2 catalogue

We compare the estimated redshifts of our 2938 candidates with optical counterparts (no f_{cont}^{max} applied) with those from the PSZ2 catalogue (Planck Collaboration 2016), because the two catalogues should contain a similar number of clusters at S/N>4.5, with small variations expected due to the different algorithms used to detect clusters. There are 1094 PSZ2 clusters with a measured redshift, and, out of those, 226 lie within the DES footprint. We match these 226 clusters with sources from our catalogue that have good photometric redshift estimations and S/N≥4.5, using a matching radius of 3 arcmin. In this case we do the matching using both the *Planck* SZE position and the optical positions.

We find 217 matching sources, but one of those matches does not correspond to the closest cluster in our catalogue so we exclude it and use the 216 remaining sources. Of the nine PSZ2 sources for which we find no match, seven have missing photometric information in one or more DES bands. The remaining two clusters with IDs PSZ2 G074.08-54.68 and PSZ2 G280.76-52.30 are further discussed in Appendix D.

Of this matched sample of 216 systems, 207 (214) systems have f_{cont} <0.2 (0.3) and redshifts that are in good agreement with ours. The cases of disagreement are discussed in detail in Appendix C2. By comparing the 214 matching clusters with $f_{cont} < 0.3$ to the numbers shown on the Table 1 (264 at S/N>4.5), it becomes apparent that the analysis we describe here has led to photometric redshifts and optical counterparts for 50 PSZ2 clusters that previously had no redshift information. Fig. 7 shows the redshift distribution of our cluster catalogue (red histogram) and of the PSZ2 catalogue within DES (blue histogram).

4.3.2 PSZ-MCMF mass-redshift distribution

We compare the mass-redshift distribution of PSZ-MCMF clusters with that of MARD-Y3, *SPT*, and PSZ2. Our first step in cross-matching is to select clusters that are the closest to their respective optical counterpart (853 clusters). Then the cross-match comparison is done by using both a positional match within 3 arcmin from the *Planck* positions or from the optical positions. We also add a redshift constraint, where only candidates with a redshift offset $\delta z < 0.02$ (using only the first peak) are considered. This gives a total of 500,
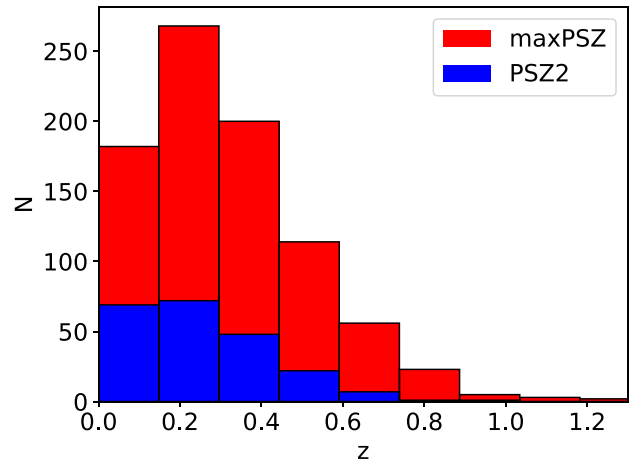

Figure 7. Redshift distribution of the PSZ-MCMF clusters (red) and the PSZ2 clusters within the DES region (blue). The new PSZ-MCMF catalogue presented here is significantly larger and extends to higher redshift.

187, and 233 matches with MARD-Y3, PSZ2, and *SPT* (2500 d + ECS), respectively. In total, then, 329 PSZ-MCMF clusters are not matched to any of the three published catalogues.

In Fig. 8 we show the mass versus redshift distribution for the different cluster samples. The *SPT*, PSZ2, and MARD-Y3 samples are shown as green stars, blue diamonds, or grey squares, respectively. PSZ-MCMF clusters are shown with red dots if they are unmatched to clusters in *SPT*, PSZ2, or MARD-Y3 and as black circles if they are matched. The red systems are the previously unknown SZE selected clusters in the DES region. In the case of matches to previously published samples, we adopt the mass and redshift estimates from the PSZ-MCMF sample to ensure the points lie on top of one another. Fig. 8 contains more than 10 massive clusters ($M_{500} \gtrsim 10^{15}$ M$_\odot$ and $z < 0.5$) with no matches to the PSZ-MCMF cluster sample. Visual inspection shows that those systems were slightly outside the DES footprint or within masked regions within the general DES footprint.

For MARD-Y3, we clean the unmatched sources by selecting those without multiple X–ray sources to avoid double counting clusters, and also exclude clusters with strong active galactic nucleus (AGN) contamination as indicated by their AGN exclusion filter (see section 4.2.1 in Klein et al. 2019). Also, following their mass versus redshift distribution, we use a threshold of $f_{cont} < 0.05$ and also remove sources with a second counterpart with $f_{cont} < 0.05$.

The mass-redshift distribution of our *Planck* sample is similar to that of the MARD-Y3 X–ray selected sample, which finds more lower mass systems at lower redshifts. In contrast, the *SPT* sample mass-redshift distribution exhibits only a slight redshift trend (Bleem et al. 2015), but it lacks the lower mass systems seen at low redshift in the *Planck* and MARD-Y3 samples. For the *Planck* selection, it is the multifrequency mapping that enables the separation of the thermal SZE from the contaminating CMB primary temperature anisotropy, and this enables the detection of low redshift and low mass systems in a way that resembles the flux limited selection in the MARD-Y3 catalogue. *SPT*, on the other hand, has coverage over a narrow range of frequency and cannot as effectively separate the thermal SZE and the primary CMB anisotropies. The *SPT* cluster extraction is therefore restricted to a smaller range of angular scales, which is well matched to cluster virial regions at $z \gtrsim 0.3$, but at lower redshifts an ever smaller fraction of the SZE signature is obtained, making it ineffective at detecting the low mass and low redshift
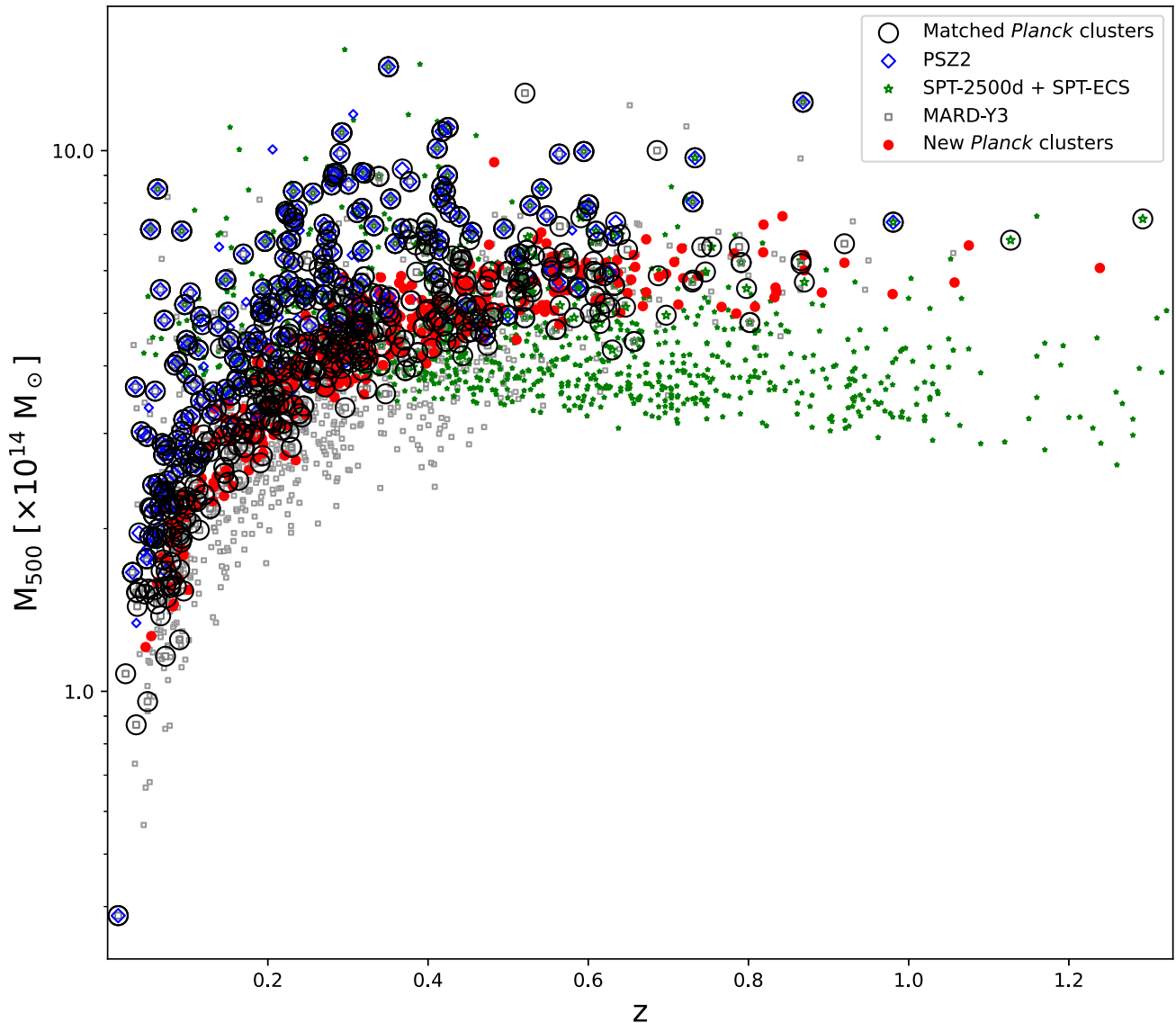
Figure 8. Mass versus redshift for the different cluster samples MARD-Y3, PSZ2, *SPT*, and the PSZ-MCMF cluster catalogue. *SPT*, PSZ2, and MARD-Y3 clusters are shown as green stars, blue diamonds, or grey squares, respectively. New PSZ-MCMF clusters identified in this analysis (no match to PSZ2, *SPT*, or MARD-Y3) are shown with red dots whereas clusters that match with at least one of the other catalogues appear as black circles. In the case of matches, masses and redshifts are those of our PSZ-MCMF catalogue.

systems seen in the *Planck* and MARD-Y3 samples. At $z \lesssim 0.6$, MARD-Y3 selects lower mass clusters than we are able to with our *Planck* sample, but at higher redshifts both catalogues follow similar distributions. When comparing with PSZ2, our new *Planck* catalogue contains lower mass clusters at all redshifts, which is expected given that we are pushing to lower S/N with our *Planck* catalogue. Our *Planck* sample also contains the first $z > 1$ *Planck*-selected clusters.

4.4 PSZ-MCMF contamination and incompleteness

An application of the *Planck*-based cluster finding algorithm to mock data suggests that at S/N>3 we should expect about 75 per cent of the candidates to be contamination (noise fluctuations; see Section 2.2). In this section we explore that expectation using information from the MCMF followup. Moreover, as one subjects the confirmed PSZ-

MCMF sample to more restrictive f_{cont} selection thresholds (i.e. smaller values), one is removing not only chance superpositions (contaminants) from the sample, but also some real clusters. In the following subsections we also explore the incompleteness introduced by the f_{cont} selection.

4.4.1 Estimating contamination

With the MCMF analysis results in hand, we can now estimate the true contamination fraction of the initial candidate list by analysing the number of real cluster candidates N_{real} from the number of selected clusters N_{cl} as a function of the f_{cont} threshold f_{cont}^{max} and input *Planck* candidate catalogue contamination $f_{SZE-cont}$. The number of real clusters is estimated as

$$N_{real}(f_{cont}^{max}) = N_{cl}(f_{cont} < f_{cont}^{max}) \left[1 - f_{cont}^{max} f_{SZE-cont}\right], \quad (5)$$

where $N_{cl}(f_{cont} < f_{cont}^{max})$ is the total number of confirmed *Planck* candidates with $f_{cont} < f_{cont}^{max}$ and $\left[1 - f_{cont}^{max} f_{SZE-cont}\right]$ represents the fraction of real clusters in a sample of MCMF confirmed clusters. As discussed in Section 3.2.2, f_{cont} is defined in a cumulative manner and the final contamination of an $f_{cont} < f_{cont}^{max}$ selected sample is the product $f_{cont}^{max} f_{SZE-cont}$ where $f_{SZE-cont}$ is the contamination fraction of the original *Planck* candidate list, and f_{cont}^{max} is the fraction of this contamination that makes it into the final confirmed cluster sample.

In this way, we can estimate N_{real} for a number of values of f_{cont}^{max} and $f_{SZE-cont}$. Under the assumption that the f_{cont} selection restricts contamination as expected, we can then solve for the input candidate list contamination $f_{SZE-cont}$, which again was estimated through *Planck* sky simulations to be ∼0.75. The catalogue contamination should give a constant ratio of $N_{real}/N_{cand} = 1 - f_{SZE-cont}$ at higher f_{cont}^{max} where this f_{cont} selection becomes unimportant.

It is instructive to start with a less contaminated sample similar to PSZ2 by taking into account only *Planck* candidates with S/N>4.5 (284 candidates). In Fig. 9 we plot the ratio of the number of estimated real clusters N_{real} to the total number of *Planck* candidates as a function of the f_{cont} threshold value f_{cont}^{max} used to select the sample. Each solid curve represents the estimated number of real clusters N_{real}, colour coded according to the assumed *Planck* candidate sample contamination $f_{SZE-cont}$. The horizontal dashed lines show $1 - f_{SZE-cont}$, which is showing the fraction of *Planck* candidates that are expected to be real clusters and therefore could be confirmed using MCMF. We would expect that for threshold values f_{cont}^{max} approaching 1, where the MCMF selection is having no impact, that the fraction plotted in the figure would reach the value $1 - f_{SZE-cont}$.

The input contamination that best describes the high S/N sample is $f_{SZE-cont} = 8.5$ per cent, where at $f_{cont} < 0.3$ the fraction of confirmed candidates has reached the maximum possible within the *Planck* candidate list. A further relaxing of the f_{cont} threshold has essentially no impact on the number of real clusters N_{real}; it just adds contaminants to the list of MCMF confirmed clusters N_{cl} at just the rate that matches the expected increase in contamination described in equation (5). This contamination is in line with the ∼ 91 per cent reliability estimated for the PSZ2 cluster cosmology sample (see fig. 11 in Planck Collaboration 2016).

Note the behavior of the blue line at f_{cont} values <0.3. The confirmed ratio falls away from 90 per cent, indicating the onset of significant incompleteness in the MCMF selected sample. This is an indication that as one uses f_{cont} to produce cluster samples with lower and lower contamination fractions, one is also losing real systems and thereby increasing incompleteness. We discuss this further in the next subsection (Section 4.4.2).

For the more contaminated S/N>3 *Planck* candidate sample (2913 candidates) the results are shown in the bottom panel of Fig. 9. When the f_{cont} threshold is 0.2, the estimated number of real clusters N_{real} is roughly 25 per cent of the total number of *Planck* candidates, which implies a 75 per cent contamination. However, unlike the S/N>4.5, the curve does not flatten until $f_{cont} \geq 0.65$, and only for initial contamination values $f_{SZE-cont} = 50$ per cent. This later flattening reflects the low mass range (and therefore lower richness range) of the S/N>3 candidate list. Additionally, our analysis indicates that the initial contamination of the *Planck* S/N>3 candidate list is ≈51 per cent rather than the estimated 75 per cent from *Planck* mock sky experiments. We explore these differences further in Appendix E.

Finally, using this 51 per cent initial contamination (yellow lines), we expect to lose 286 clusters when going from an f_{cont} threshold of <0.2 (∼90 per cent purity) to <0.05 (∼97.5 per cent purity). Indeed, any f_{cont} threshold below 0.6 will remove real *Planck*-selected clusters from the MCMF confirmed sample, but including these systems comes
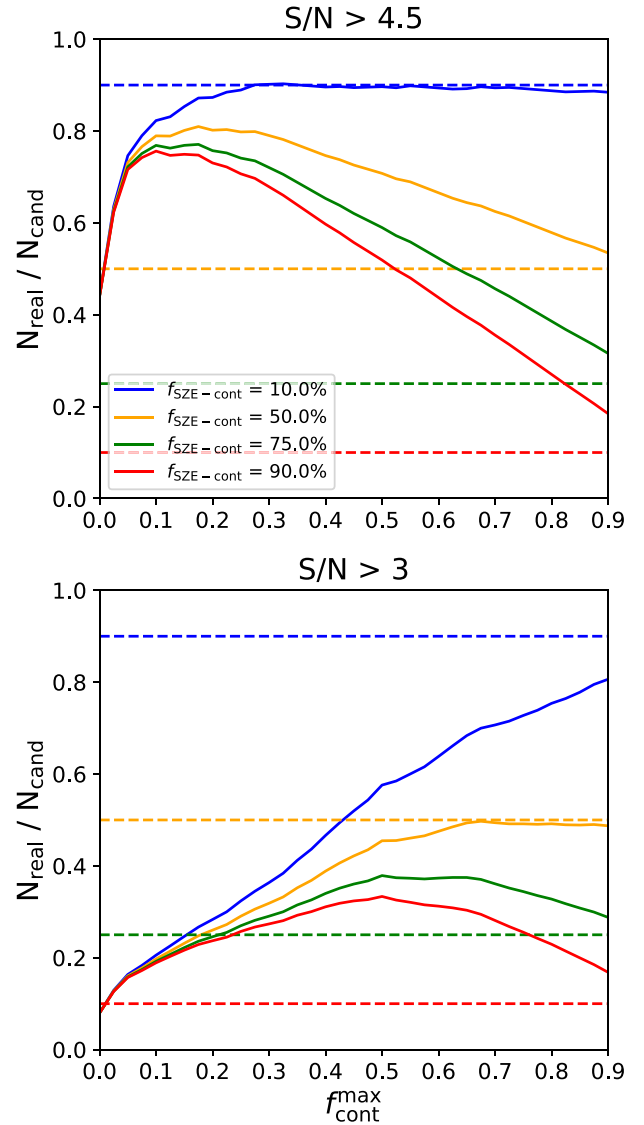

Figure 9. Ratio of the estimated number of real clusters N_{real} to the total number of candidate clusters N_{cand} in the *Planck* sample as a function of the f_{cont} threshold value applied. The solid lines show different curves from equation (5) with four different values of the contamination $f_{SZE-cont}$ of the initial *Planck* candidate list. The dashed lines show $1 - f_{SZE-cont}$, with colours encoding different initial contamination levels. The analysis indicates an initial contamination of 10 per cent in the S/N>4.5 (upper) and 50 per cent in the S/N>3 (lower) *Planck* candidate samples.

at the cost of higher contamination (purity drops to ∼70 per cent). The purity for different thresholds of f_{cont}^{max} is listed in Table 1 for the two *Planck* candidate S/N ranges.

Given how the PSZ-MCMF cluster catalogue is constructed (the combination of the low and high S/N subsamples), the final purity is estimated to be ∼90 per cent.

4.4.2 *Estimating incompleteness*

From this analysis, we can estimate the number of missed clusters N_{missed} or equivalently the fractional incompleteness for a given f_{cont} threshold. First, we estimate the maximum number of real clusters in the full sample as $N_{real, max} = N_{cand}(1 - f_{SZE-cont}) = 1427$ (for the

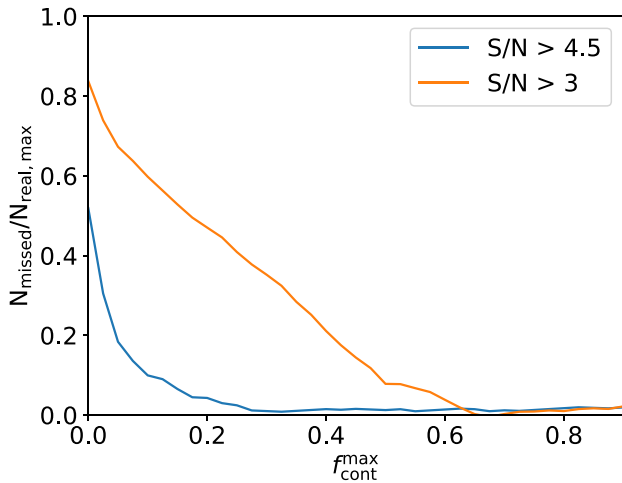**Figure 10.** Estimate of the fractional incompleteness versus the f_{cont} threshold f_{cont}^{max} for the S/N>4.5 ($f_{SZE-cont} = 8.5$ per cent) and S/N>3 ($f_{SZE-cont} = 51$ per cent) confirmed cluster samples, shown with blue and orange lines, respectively. The contamination of the resulting cluster catalogue is given by $f_{SZE-cont} f_{cont}^{max}$ (see Section 4.4.1 and Table 1).

S/N>3 sample), where in this case N_{cand} is the full *Planck* candidate list. Then, we estimate the number of missed clusters using the total number of expected real clusters minus the number of real SZE selected clusters at a particular f_{cont} threshold value,

$$N_{missed}(f_{cont} < f_{cont}^{max}) = N_{real,max} - N_{real}(f_{cont}^{max}), \quad (6)$$

where $N_{real}(f_{cont}^{max})$ is defined as in equation (5). In Fig. 10 we show the ratio of missed clusters over the expected maximum number of real clusters for the samples at S/N>3 (orange line) and S/N>4.5 (blue line). An f_{cont} threshold of 0.2 in the S/N>4.5 *Planck* sample would be missing slightly over 3 per cent of the real clusters, while at S/N>3 and the same threshold 0.2, we expect to miss ~ 47 per cent of the real clusters. With an f_{cont} threshold of 0.05 we miss ~ 70 per cent of the real clusters. The completeness for different selection thresholds f_{cont}^{max} is shown in Table 1, for the two *Planck* candidate S/N ranges. We estimate the completeness of the PSZ-MCMF cluster catalogue to be ~ 54 per cent.

The higher incompleteness for the lower S/N sample is expected, because as discussed in Section 4.2 this sample pushes to lower masses and therefore lower richnesses than the S/N>4.5 sample. At lower richness, real clusters cannot be as effectively differentiated from the typical background richness distribution (see random line-of-sight discussion in Section 3.2). In this low mass regime, along with the large positional uncertainties, the cost of creating a higher purity *Planck* sample is the introduction of high incompleteness.

5 SUMMARY AND CONCLUSIONS

In this analysis we create the PSZ-MCMF cluster catalogue by applying the MCMF cluster confirmation algorithm to DES photometric data and an SZE selected cluster candidate list extracted down to S/N = 3 from *Planck* sky maps. In contrast to previous analyses employing the MCMF algorithm, the low angular resolution of *Planck* together with the low S/N threshold result in much larger positional uncertainties of the SZE selected candidates. To overcome this challenge we apply the MCMF algorithm twice, first using the *Planck* candidate coordinates to define a search region with an aperture that is three times the *Planck* candidate positional uncertainty, and then second using the

positions of the optical counterparts found in the first run, with an aperture based on an estimate of the halo radius $R_{500}(z)$ that employs the mass constraints from the *Planck* data set.

We control the contamination of the final, confirmed sample by measuring the parameter f_{cont} for each *Planck* candidate. As discussed in Section 3.2.2, the value of this parameter is proportional to the probability that the *Planck* candidate and its optical counterpart are a chance superposition of physically unassociated systems rather than a real cluster of galaxies. About 10 per cent of the *Planck* candidates exhibit multiple potential optical counterparts. In such cases we select the most likely optical counterpart by choosing the one with the lowest f_{cont} value (lowest chance of being contamination).

Our analysis of the PSZ-MCMF sample indicates that the initial contamination fraction of the *Planck* S/N>4.5 candidate list is $f_{SZE-cont} \sim 9$ per cent and the S/N>3 candidate list is $f_{SZE-cont} \sim 50$ per cent. The optical followup with MCMF allows us to reduce this contamination substantially to the product $f_{cont}^{max} \times f_{SZE-cont}$, where f_{cont}^{max} is the maximum allowed f_{cont} value in a particular subsample.

Table B1 contains the full PSZ-MCMF sample of 853 confirmed clusters, defined using an f_{cont} threshold of 0.3 for S/N>4.5 candidates and an f_{cont} threshold of 0.2 for S/N>3 candidates. Table 1 contains the number of clusters, the purity and the completeness of this cl catalogue (in bold face) together with other subsamples constructed using smaller f_{cont} thresholds of 0.2, 0.1, and 0.05 for both *Planck* S/N ranges. Whereas the full catalogue contains 853 clusters with a purity of 90 per cent and completeness of 54 per cent, the subsample with $f_{cont} <0.2$ (<0.1) contains 842 (604) clusters with purity and completeness of 90 per cent (95 per cent) and 53 per cent (40 per cent), respectively.

Furthermore, the cl cluster sample at S/N>3 excludes 47 per cent of the real clusters when applying a limiting value at $f_{cont} < 0.2$, while the same threshold on the S/N>4.5 sample excludes around 4 per cent. We attribute the higher incompleteness of the confirmed low S/N sample to the fact that these systems have lower masses and richnesses. The lower richnesses for the real clusters in this regime are simply more difficult to separate from the characteristic richness variations along random lines of sight in the DES survey. The relatively large positional uncertainties of the *Planck* candidates makes this effect even stronger.

Users are encouraged to select subsamples of the cl sample with lower contamination, depending on their particular scientific application. The PSZ-MCMF catalogue adds 828 previously unknown *Planck* identified clusters at S/N>3, and it delivers redshifts for 50 previously published S/N>4.5 *Planck* clusters.

For each of the confirmed clusters we derive photometric redshifts. By comparing the PSZ-MCMF cluster sample with spectroscopic redshifts from the literature, we find a mean redshift offset $<10^{-4}$ and an RMS scatter of 0.47 per cent. With these redshifts together with the *Planck* mass constraints, we estimate halo masses for all confirmed clusters. These original *Planck*-based mass estimates contain no correction for hydrostatic mass bias, and so these are rescaled by the factor $1/0.8 = 1.25$ to make them consistent with the weak lensing derived *SPT* cluster masses (Bocquet et al. 2019). Optical positions, redshifts, and halo masses M_{500} are provided for each confirmed cluster in Table B1.

We crossmatch the PSZ-MCMF cluster catalogue to different SZE and X-ray selected cluster catalogues within the DES footprint. We find that the PSZ-MCMF mass distribution with redshift is similar to that of the X–ray selected MARD-Y3 cluster catalogue. However, at redshifts lower than $z < 0.5$ the PSZ-MCMF catalogue does not contain the lower mass systems that the X-ray selected MARD-Y3

catalogue contains. When comparing with the previous *Planck* SZE source catalogue PSZ2, we have optical counterparts for most of the systems that lie within the DES footprint, finding in general good agreement with their previously reported redshifts. Compared to the higher S/N PSZ2 sample, we find that most of our new lower S/N PSZ-MCMF systems lie at lower masses at all redshifts and extend to higher redshift, as expected. Probing to lower masses allows for the confirmation of the first $z > 1$ *Planck* identified galaxy clusters. Crudely scaling these results to the full extragalactic sky ($\sim$30 000 deg^2) implies that the *Planck* full sky candidate list confirmed using MCMF applied to DES like multiband optical data would yield a sample of $\sim$6000 clusters, which is $\sim$6 times the number of clusters in the PSZ2 all-sky cluster catalogue with redshift information.

DATA AVAILABILITY

The optical data underlying this article corresponds to the DES Y3A2 GOLD photometric data, which is available through the DES data management website.[5] The full PSZ-MCMF cluster catalogue (1092 clusters) will be made available online at the VizieR archive.

REFERENCES

Abbott T. et al., 2016, MNRAS, 460, 1270
Abbott T. M. C. et al., 2018, ApJS, 239, 18
Abbott T. M. C. et al., 2021, ApJS, 255, 20
Aghanim N. et al., 2015, A&A, 580, A138
Arnaud M., Pratt G. W., Piffaretti R., Böhringer H., Croston J. H., Pointecouteau E., 2010, A&A, 517, A92
Bleem L. E. et al., 2015, ApJS, 216, 27
Bleem L. E. et al., 2020, ApJS, 247, 25
Bocquet S. et al., 2019, ApJ, 878, 55
Böhringer H. et al., 2004, A&A, 425, 367
Brunner H. et al., 2022, A&A, 661, A1
Carlstrom J. E. et al., 2011, PASP, 123, 568
Crocce M., Castander F. J., Gaztañaga E., Fosalba P., Carretero J., 2015, MNRAS, 453, 1513
DeRose J. et al., 2019, preprint (arXiv:1901.02401)
Delabrouille J. et al., 2013, A&A, 553, A96
Drlica-Wagner A. et al., 2018, ApJS, 235, 33
Finoguenov A. et al., 2020, A&A, 638, A114
Flaugher B. et al., 2015, AJ, 150, 150
Gladders M. D., Yee H. K. C., Majumdar S., Barrientos L. F., Hoekstra H., Hall P. B., Infante L., 2007, ApJ, 655, 128
Grandis S. et al., 2020, MNRAS, 498, 771
Grandis S. et al., 2021, MNRAS, 504, 1253
Herranz D., Sanz J. L., Hobson M. P., Barreiro R. B., Diego J. M., Martínez-González E., Lasenby A. N., 2002, MNRAS, 336, 1057
High F. W. et al., 2010, ApJ, 723, 1736
Hilton M. et al., 2021, ApJS, 253, 3
Hoekstra H., Herbonnet R., Muzzin A., Babul A., Mahdavi A., Viola M., Cacciato M., 2015, MNRAS, 449, 685
Klein M. et al., 2018, MNRAS, 474, 3324

[5]https://des.ncsa.illinois.edu/

Klein M. et al., 2019, MNRAS, 488, 739
Klein M. et al., 2022, A&A, 661, A4
Koulouridis E. et al., 2021, A&A, 652, A12
Lin Y., Mohr J. J., Stanford S. A., 2004, ApJ, 610, 745
Liu J. et al., 2015, MNRAS, 449, 3370
Liu A. et al., 2022, A&A, 661, A2
McClintock T. et al., 2019, MNRAS, 482, 1352
Marriage T. A. et al., 2011, ApJ, 737, 61
Maturi M., Bellagamba F., Radovich M., Roncarelli M., Sereno M., Moscardini L., Bardelli S., Puddu E., 2019, MNRAS, 485, 498
Melin J. B., Bartlett J. G., Delabrouille J., 2006, A&A, 459, 341
Melin J. B., Bartlett J. G., Tarrío P., Pratt G. W., 2021, A&A, 647, A106
Morganson E. et al., 2018, PASP, 130, 074501
Navarro J. F., Frenk C. S., White S. D. M., 1996, ApJ, 462, 563
Navarro J. F., Frenk C. S., White S. D. M., 1997, ApJ, 490, 493
Piffaretti R., Arnaud M., Pratt G. W., Pointecouteau E., Melin J. B., 2011, A&A, 534, A109
Planck Collaboration, 2014, A&A, 571, A29
Planck Collaboration, 2016, A&A, 594, A27
Planck Collaboration, 2020, A&A, 641, A1
Rozo E., Rykoff E. S., 2014, ApJ, 783, 80
Rozo E. et al., 2009a, ApJ, 699, 768
Rozo E. et al., 2009b, ApJ, 703, 601
Rykoff E. S. et al., 2014, ApJ, 785, 104
Sheldon E. S., 2014, MNRAS, 444, L25
Song J., Mohr J. J., Barkhouse W. A., Warren M. S., Dolag K., Rude C., 2012a, ApJ, 747, 58
Song J. et al., 2012b, ApJ, 761, 22
Staniszewski Z. et al., 2009, ApJ, 701, 32
Sunyaev R. A., Zeldovich Y. B., 1972, Comment. Astrophys. Space Phys., 4, 173
von der Linden A. et al., 2014, MNRAS, 443, 1973
Wen Z. L., Han J. L., 2022, MNRAS, 513, 3946

SUPPORTING INFORMATION

Supplementary data are available at *MNRAS* online.

PSZ-SN3_cluster_catalogue.vot

Please note: Oxford University Press is not responsible for the content or functionality of any supporting materials supplied by the authors. Any queries (other than missing material) should be directed to the corresponding author for the article.

APPENDIX A: MULTIPLE OPTICAL COUNTERPARTS

In Fig. A1 we show an example of the *Planck* candidate PSZ-SN3 J0605-3519, which is classified as a candidate with multiple optical counterparts. The upper figure shows the richness as a function of redshift, which shows two prominent peaks at $z_{MCMF} = 0.15$ and $z_{MCMF} = 0.52$. The lower image contains the pseudo-colour image from *gri* DES cutouts. White and red contours are derived from the RS galaxy density map for galaxies at $z_{MCMF} = 0.15$ and $z_{MCMF} = 0.52$, respectively. The richness for these two counterparts are $\lambda_{MCMF} = 84$ and $\lambda_{MCMF} = 156$ for the white and red contours, for the two optical candidates at $z_{MCMF} = 0.15$ and $z_{MCMF} = 0.52$, respectively. For this candidate, the estimated f_{cont} of both redshift peaks is 0, indicating a vanishing small probability that either one is a random superposition. We choose the one at $z_{MCMF} = 0.15$ as the 'preferred' counterpart because it lies nearer to the *Planck* candidate position. The reported spectroscopic redshift for this cluster comes from the REFLEX cluster catalogue, with $z_{spec} = 0.1392$ for cluster RXCJ0605.8-3518 (Böhringer et al. 2004).
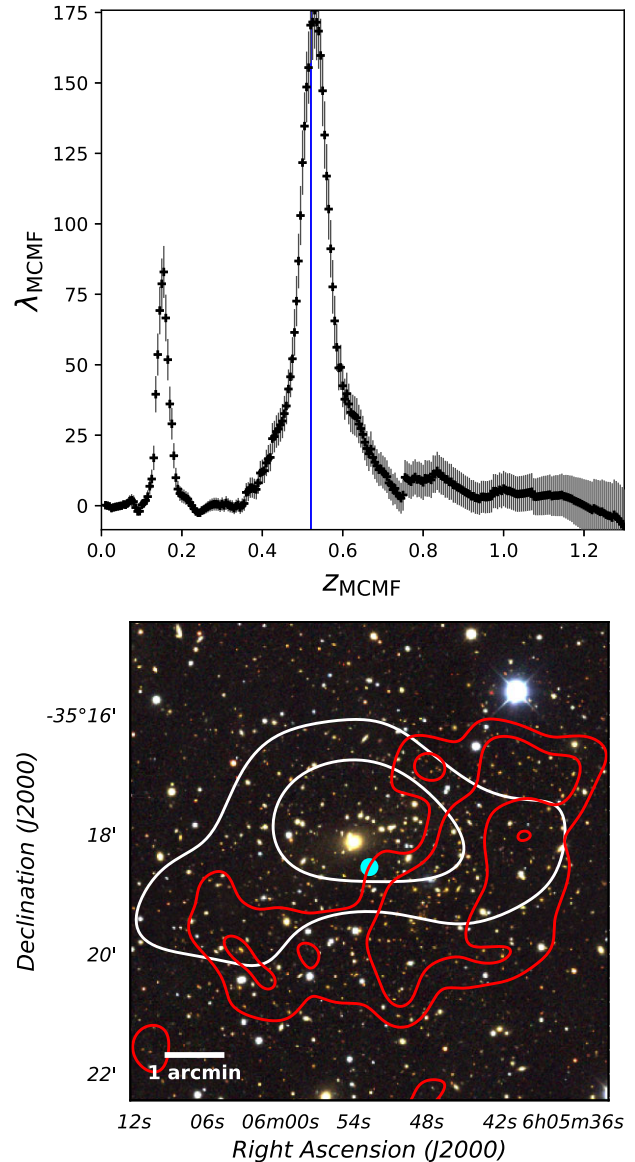
Figure A1. *Top*: Richness as a function of redshift for the *Planck* candidate PSZ-SN3 J0605-3519. Two richness peaks at $z_{MCMF} = 0.15$ and $z_{MCMF} = 0.52$ are evident. *Bottom*: Pseudo-colour image from DES *g, r, i* cutouts around the *Planck* candidate coordinates, marked by a cyan dot. Contours are from the galaxy density maps of the counterpart at $z_{MCMF} = 0.15$ (white) and at $z_{MCMF} = 0.52$ (red).

APPENDIX B: SHARED OPTICAL COUNTERPART

In Fig. B1 we show an example of two *Planck* candidates (PSZ-SN3 J2248-4430 with $f_{cont} = 0.00$ and PSZ-SN3 J2248-4436 with $f_{cont} = 0.18$) sharing the same optical counterpart, where the *Planck* positions are marked with dots. The optical centre of the preferred counterpart for each candidate is marked with a cross of the same colour. White contours are the RS galaxy density map from the first MCMF run, where the optical centres are determined. Both redshifts point toward a cluster at $z_{MCMF} = 0.35$, but it is pretty clear that the two *Planck* candidates have resolved to the same optical counterpart. Interestingly, this optical system also corresponds to a

Table B1. 30 entries of the new PSZ-MCMF cluster catalogue, limited to the most important columns of the catalogue.

Name	RA_{Planck} deg.	$Dec._{Planck}$ deg.	S/N	σ_{pos} arcmin	RA^* deg.	$Dec.^*$ deg.	σ_{SZ-Op}^*	z_{MCMF}^*	λ_{MCMF}^*	f_{cont}^*	M_{500} $\times 10^{14}$ M$_\odot$	FLAG COSMO	FLAG CLEAN	FLAG QNEURAL
PSZ-SN3 J0543-1857	85.9328	-18.9048	3.8526	5.5398	85.9314	-18.9595	0.5922	0.6568	83.1978	0.0530	6.4115	1	1	1
PSZ-SN3 J0550-2233	87.6461	-22.6607	3.4805	6.9070	87.6388	-22.5545	0.9247	0.0801	34.5207	0.0476	1.9277	1	1	1
PSZ-SN3 J0548-2152	87.1619	-21.9176	4.0710	6.7710	87.0182	-21.8678	1.2612	0.0862	42.4760	0.0197	2.3530	1	1	1
PSZ-SN3 J0558-2629	89.7651	-26.5085	4.2204	6.1337	89.7495	-26.4901	0.2257	0.2681	84.8770	0.0000	4.4636	1	1	1
PSZ-SN3 J0555-2637	88.8111	-26.6496	3.3028	5.2495	88.8133	-26.6195	0.3446	0.2766	71.8997	0.0000	3.9173	1	1	1
PSZ-SN3 J0554-2556	88.7011	-25.9919	3.0569	5.5877	88.6952	-25.9386	0.5750	0.2714	54.1370	0.0505	3.6558	1	1	1
PSZ-SN3 J0616-3948	94.1341	-39.8328	8.7490	2.5549	94.1227	-39.8033	0.7235	0.1506	41.0926	0.0545	5.0250	1	1	1
PSZ-SN3 J0609-3700	92.4479	-36.9542	3.9032	4.9092	92.4358	-37.0106	0.6994	0.2685	72.3089	0.0000	4.1736	1	1	1
PSZ-SN3 J0638-5358	99.7055	-53.9805	13.5941	2.3905	99.6977	-53.9745	0.1891	0.2320	92.2980	0.0000	8.4066	1	1	1
PSZ-SN3 J2118+0033	319.7380	0.5439	4.8582	2.2707	319.7118	0.5598	0.8107	0.2686	97.6065	0.0000	5.4214	1	1	1
PSZ-SN3 J2119+0120	319.9540	1.3562	3.9086	4.4458	319.9744	1.3381	0.3680	0.1237	31.1533	0.0955	2.8914	1	1	1
PSZ-SN3 J0514-1951	78.6623	-19.9231	4.1396	4.9319	78.6868	-19.8534	0.8936	0.1357	48.7245	0.0156	3.3206	1	1	1
PSZ-SN3 J0502-1813	75.7216	-18.1993	3.4844	5.6044	75.6171	-18.2214	1.0885	0.5749	60.3850	0.1406	5.5214	1	1	1
PSZ-SN3 J0548-2530	87.1631	-25.4926	6.3700	5.4270	87.1715	-25.5048	0.1593	0.0311	36.2221	0.0431	1.6597	1	1	1
PSZ-SN3 J0528-2942	82.0841	-29.7250	5.7007	3.8145	82.0811	-29.7101	0.2386	0.1583	40.3784	0.0691	4.1431	1	1	1
PSZ-SN3 J0538-2038	84.5847	-20.6454	5.4451	4.9996	84.5856	-20.6370	0.1010	0.0871	37.0128	0.0421	2.9113	1	1	1
PSZ-SN3 J0520-2625	80.1255	-26.4429	4.9942	1.7900	80.1125	-26.4237	0.7537	0.2790	77.4486	0.0000	5.2686	1	1	1
PSZ-SN3 J0516-2237	79.2379	-22.6223	4.9108	4.2022	79.2386	-22.6249	0.0390	0.2949	98.6374	0.0000	5.6110	1	1	1
PSZ-SN3 J0529-2253	82.4507	-22.8641	4.4810	5.8471	82.4575	-22.8849	0.2227	0.1776	57.6785	0.0221	3.7982	1	1	1
PSZ-SN3 J0516-2521	79.1042	-25.3215	4.4406	6.2807	79.0631	-25.3624	0.5279	0.2808	56.1890	0.0331	4.6955	1	1	1
PSZ-SN3 J0519-2056	80.0775	-21.0020	3.8548	5.1985	79.9872	-20.9448	1.1760	0.3039	77.7563	0.0000	4.9633	1	1	1
PSZ-SN3 J0540-2127	85.1922	-21.4732	3.5656	5.4369	85.2095	-21.4615	0.2195	0.5242	77.4497	0.0461	5.7749	1	1	1
PSZ-SN3 J0521-2754	80.3559	-27.9377	3.9751	3.6068	80.3628	-27.9156	0.3821	0.3150	98.6217	0.0000	4.7847	1	1	1
PSZ-SN3 J0545-2556	86.3885	-25.9053	4.0783	5.5571	86.3658	-25.9377	0.4132	0.0469	37.0815	0.0371	1.5132	1	1	1
PSZ-SN3 J0533-2823	83.5642	-28.3836	3.7296	5.2059	83.4791	-28.3934	0.8706	0.1916	49.4947	0.0542	3.1730	1	1	1
PSZ-SN3 J0530-2226	82.6648	-22.4653	4.5761	3.3990	82.6643	-22.4453	0.3528	0.1680	71.5937	0.0067	3.6625	1	1	1
PSZ-SN3 J0546-2410	86.6542	-24.1719	3.1268	5.3599	86.5557	-24.1669	1.0076	0.3247	46.8889	0.0797	4.1055	1	1	1
PSZ-SN3 J0530-2556	82.6693	-25.7861	3.1967	5.1885	82.7240	-25.9483	1.9600	0.1926	49.8588	0.0535	2.9369	1	1	1
PSZ-SN3 J0605-3519	91.4696	-35.3091	15.2181	2.3889	91.4492	-35.3206	0.5087	0.5210	155.6621	0.0000	12.7754	1	1	1
PSZ-SN3 J0553-3342	88.3485	-33.7020	13.0358	1.6357	88.3436	-33.7078	0.2613	0.4174	146.0235	0.0000	10.8541	1	1	1

The full cluster catalogue containing 853 clusters will be available online via *VizieR* server at CDS (http://vizier.u-strasbg.fr) and as supplementary material, including additional columns. The first five columns show the cluster name, the *Planck* position, the S/N, and the positional uncertainty of the candidates. The next columns are $_{MCMF}$ derived quantities for the most likely optical counterpart (lowest f_{cont}). These are: (6 and 7) the optical position of the cluster, (8) the distance between the optical and the *Planck* positions normalized by the positional uncertainty, (9) the redshift, and (10) the richness. Column (11) is the estimated probability that the source is a random superposition and column (12) contains the mass estimate M_{500}. Columns (13–15) contain flags that are described in the text. *In the case of a second prominent optical counterpart (with $f_{cont} < 0.3$) at a different z_{MCMF}, we provide an entry for that counterpart as well. † Masses derived in Section 4.2 are divided by 0.8 to correct for the estimated hydrostatic mass bias.
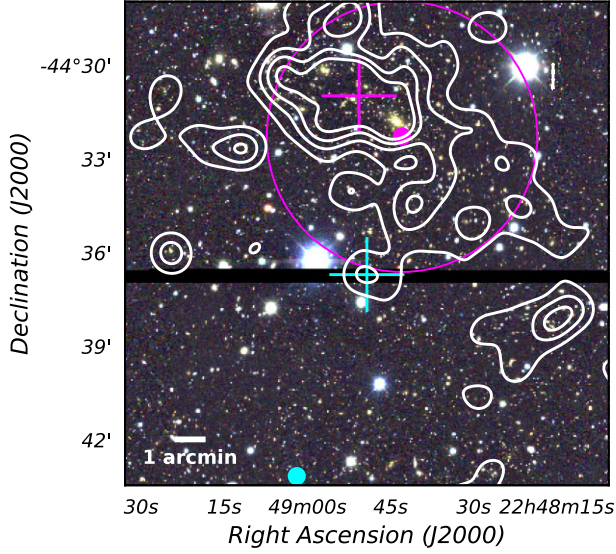
Figure B1. Pseudo-colour image from DES *g*, *r*, *i* cutouts around the coordinates of *Planck* candidates PSZ-SN3 J2248-4430 and PSZ-SN3 J2248-4436, marked by magenta and cyan dots, respectively. White contours are from the galaxy density maps of the counterpart at $z_{\rm MCMF} = 0.35$. Crosses mark the position of the optical counterparts associated with each of the *Planck* sources, colour coded according to the *Planck* source.

South Pole Telescope (*SPT*) cluster, namely SPT-CL J2248-4431, with a spectroscopic redshift of $z_{\rm spec} = 0.351$ (Bocquet et al. 2019).

To resolve such cases, we select the *Planck* candidate with the smallest projected distance from the optical centre normalized by the positional uncertainty of the *Planck* candidate. We add a column to the catalogue that identifies which *Planck* candidate is the most likely SZE counterpart, flag$_{\rm closest}$, with a value of 0 for candidates pointing to a unique optical counterpart and 1 for candidates which share the optical counterpart with another candidate but are selected as the most likely SZE –counterpart. We visually inspected each of the 41 ($f_{\rm cont} < 0.3$) cases, looking not only at the separation, but also at the S/N of the candidates, and the estimated $f_{\rm cont}$ and λ. The method described above correctly identifies the most likely candidate for a counterpart in 18 out of 20 cases for candidates at $f_{\rm cont} < 0.3$. For the remaining two, we manually select the most likely SZE source. The final PSZ-MCMF cluster catalogue contains 853 clusters, which are the most likely SZE counterparts of their respective optical counterpart.

APPENDIX C: REDSHIFT COMPARISONS

C1 Spectroscopic redshifts

As discussed in Section 4.1.5, the full cross-matched sample contains two sources that have no significant secondary peak and exhibit a large redshift offset with respect to $z_{\rm MCMF}$. We inspect the DES images of these two clusters, namely PSZ-SN3 J2145-0142 ($z_{\rm MCMF} = 0.36$ and $f_{\rm cont} = 0.0$) and PSZ-SN3 J2347-0009 ($z_{\rm MCMF} = 0.26$ and $f_{\rm cont} = 0.02$), where the separation between the spectroscopic and optical counterparts are ∼150 and ∼180 arcsec, respectively, and find that in both cases the spectroscopic redshift points towards a different structure. In the case of PSZ-SN3 J2145-0142, the spectroscopic redshift seems to be associated with a single galaxy. Fig. C1 shows the richness as a function of redshift for both PSZ-SN3 J2145-0142
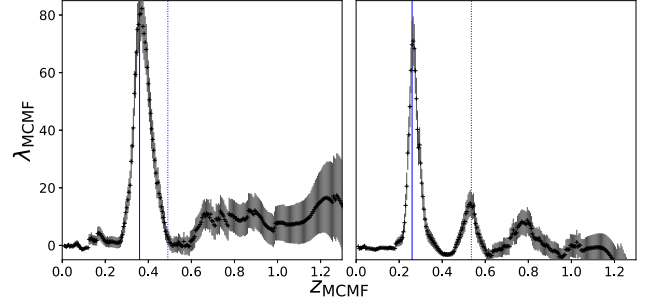

Figure C1. Richness as a function of redshift for PSZ-SN3 J2145-0142 (left) and PSZ-SN3 J2347-0009 (right). The PSZ-MCMF redshift is shown with a blue continuous line, while the spec-*z* is shown with a blue dotted line for both cases.
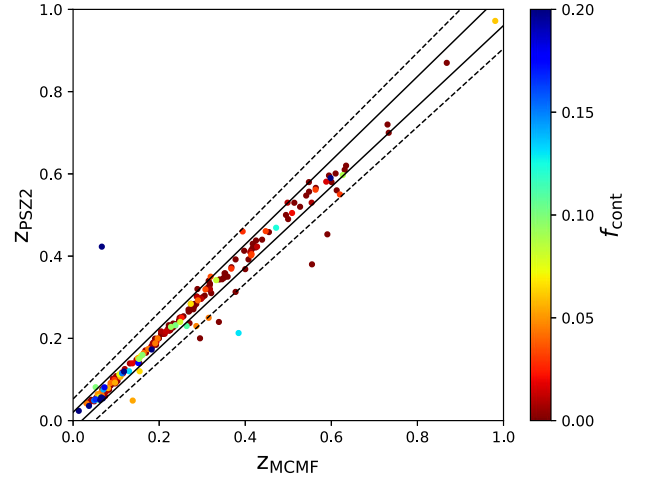

Figure C2. Comparison of MCMF photometric redshifts and those listed in the PSZ2 catalogue for the 216 matching clusters. Each cluster is colour coded by the estimated $f_{\rm cont}$, saturated at $f_{\rm cont} = 0.2$. The solid and dashed lines enclose the areas where $|(z_{\rm MCMF} - z_{\rm PSZ2}) \times (1 + z_{\rm PSZ2})^{-1}| \leq 0.02$, 0.05, respectively.

(left) and PSZ-SN3 J2347-0009 (right), with the spec-*z* marked with blue dotted lines. In the case of PSZ-SN3 J2347-0009, the measured $f_{\rm cont}$ for the structure at $z \approx 0.53$ is greater than our $f_{\rm cont}^{\rm max} = 0.3$ threshold, indicating that this is not a significant richness peak.

C2 PSZ2 redshifts

In Fig. C2 we show the comparison of PSZ2 redshifts to the MCMF for the 216 matching systems. On the x-axis, we show the photometric redshift from MCMF, while redshifts from the PSZ2 catalogue are shown on the y-axis. Each source is colour-coded according to their $f_{\rm cont}$ estimation. Continuous (dotted) lines show the enclosed area where $\delta z = |(z_{\rm MCMF} - z_{\rm PSZ2}) \times (1 + z_{\rm PSZ2})^{-1}| \leq 0.02$ (0.05). In case of multiple prominent redshift peaks with $f_{\rm cont} < 0.2$, we choose to plot only the redshift peak with the smaller δz for each match.

Fig. C2 shows that, although most of the estimated MCMF redshifts have Δz offsets at 2 per cent level or less in comparison to the PSZ2 catalogue, there are some clusters with a higher offset or with $f_{\rm cont} \geq 0.2$. Out of the 216 matching clusters, 207 have $f_{\rm cont} < 0.2$, and 197 (205) have a redshift offset, with respect to the first redshift peak, lower than 2 per cent (5 per cent). If we consider also structures with a second peak, we get 201 (209) matches with an offset lower than 2

per cent (5 per cent). To further study the reasons for these catalogue discrepancies, we separate between high f_{cont} (>0.2) and high δz (>0.05).

First, out of the nine clusters with $f_{cont} \geq 0.2$, eight have redshift offsets $\delta z < 0.02$, with seven of them having $0.2 \lesssim f_{cont} \lesssim 0.3$. DES images with artifacts such as missing bands can impact the MCMF estimation of the photometric redshifts or the cluster centres. The MCMF algorithm includes a masking of regions with artifacts when generating the galaxy density maps, thus avoiding the region entirely. Bright saturated stars can also bias the estimations of the richness and centres depending on where they are located. Thus, MCMF also masks areas with bright saturated stars for the estimation of the different parameters.

Out of the 11 matches with $\delta z > 0.05$, four have a second significant richness peak that is in agreement with the reported redshift from the PSZ2 catalogue. Of the remaining seven, one has a masked area due to a bright star. For the others, the correct counterpart (and therefore redshift) is a matter of debate. For one of the systems, the MCMF analysis finds a peak at the PSZ2 redshift, although the estimated f_{cont} is 0.31, indicating that this counterpart has a much higher probability of being contamination as compared to the primary richness peak with $f_{cont} = 0.05$.

APPENDIX D: PSZ2 COMPARISON EXAMPLES

There are two PSZ2 clusters for which we do not find a match (see Section 4.3.1) in our list of optical counterparts: PSZ2 G074.08-54.68 and PSZ2 G280.76-52.30. PSZ2 G074.08-54.68 is a cluster at $z_{PSZ2} = 0.305$, with $M_{500} = 5.40 \times 10^{14} M_\odot$ and S/N = 6.1, which is within the DES footprint and that shows a prominent optical counterpart at (RA, Dec.) = 347.04601, −1.92133, with the redshift coming from the REFLEX catalogue (ID: RXC J2308.3-0155). The area around this cluster is not masked due to bright stars or missing DES data. Nevertheless, this cluster is not in our *Planck* SZE candidate catalogue. The PSZ2 cluster catalogue is a combination of three detection methods; PowellSnakes, MMF1, and MMF3, with the latter being the one used in this work. PSZ2 G074.08-54.68 is detected by the PowellSnakes algorithm, but not by MMF1 or MMF3. This could be due to the PSZ2 cluster being close to another cluster, PSZ2 G073.82-54.92, which might have been detected first, masking part (or all) of the flux of PSZ2 G074.08-54.68.

PSZ2 G280.76-52.30 is at $z_{PSZ2} = 0.59$, with $M_{500} = 4.88 \times 10^{14}$ M$_\odot$ and S/N = 4.5, and it has the closest *Planck* SZE position from our catalogue at 3.4 arcmin, with the optical position of that candidate having an offset of 5.8 arcmin to the PSZ2 G280.76-52.30 source. Thus, it lies just outside our 3 arcmin matching radius. The PSZ2 redshift comes from the *SPT* catalogue, with the *SPT* ID of this cluster being SPT-CL J0240-5952 (Bocquet et al. 2019). From the perspective of our analysis, the *Planck* candidate (PSZ-SN3 J0240-5945) has $z_{MCMF} = 0.41$, with $\lambda_{MCMF} = 79$ and an estimated $f_{cont} = 0.03$. The second redshift peak that we find is at $z_{MCMF} = 0.605$, which is closer to the PSZ2 redshift. In Fig. D1 we show (top) the richness as a function of redshift, while below we show the *gri* DES pseudo-colour image. Overlaid are the density contours at $z_{MCMF} = 0.41$ (white) and $z_{MCMF} = 0.605$ (red). The cyan cross shows the optical position found by MCMF, and the magenta cross shows the position of PSZ2. For the peak at $z_{MCMF} = 0.605$ with $\lambda_{MCMF} = 50$, we estimate $f_{cont} = 0.28$, which means that we consider this to be a candidate with a second optical counterpart (requires $f_{cont} < 0.3$). It is worth noting that, by using the same cross-match aperture, we find a match with the SPT-2500d catalogue (Bocquet et al. 2019), SPT-CL J0240-5946, whose reported redshift is $z_{SPT} = 0.4$.
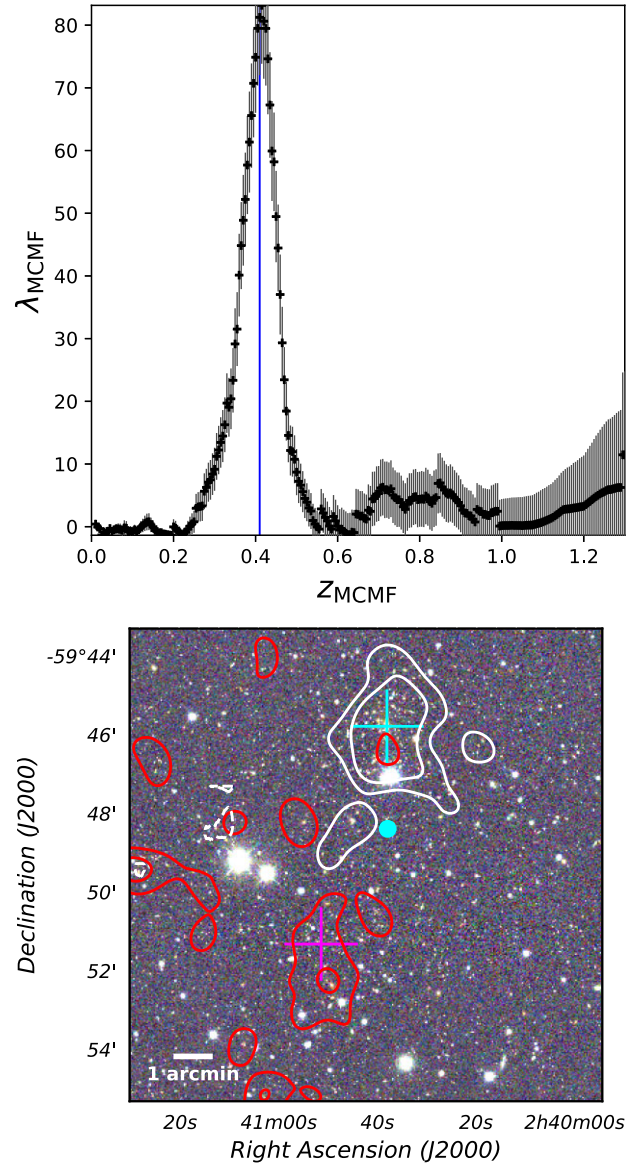

Figure D1. *Top*: Richness as a function of redshift for the *Planck* source PSZ-SN3 J0240-5945, with the best-fitting peak at $z_{MCMF} = 0.41$. *Bottom*: Pseudo-colour image from DES *g*-, *r*-, *i*-bands near the *Planck* candidate coordinates, which are marked with a cyan dot. Contours are from the galaxy density maps of the counterpart at $z_{MCMF} = 0.41$ (white) and at $z_{MCMF} = 0.605$ (red). The cyan cross marks the position of the optical counterpart found using MCMF, and the magenta cross marks the position of PSZ2 G280.76-52.30.

APPENDIX E: FURTHER EXPLORATION OF THE *Planck* CANDIDATE LIST CONTAMINATION

To investigate the difference between the observed contamination of ~51 per cent and the 75 per cent contamination estimated from the *Planck* sky simulations (see Section 2.2) we compare the detection threshold $Y_{5R500}^{min} = 2 \times 10^{-4}$ arcmin^2 to the observed Y_{5R500} distribution of our candidates. We will do this in three steps: first, we will estimate an observed mass by means of the λ_{MCMF}–M_{500} relation derived in Section E1. Secondly, we will determine the excess distribution of candidates with respect to the random lines of sight in different redshift ranges for the S/N>3 sample, which
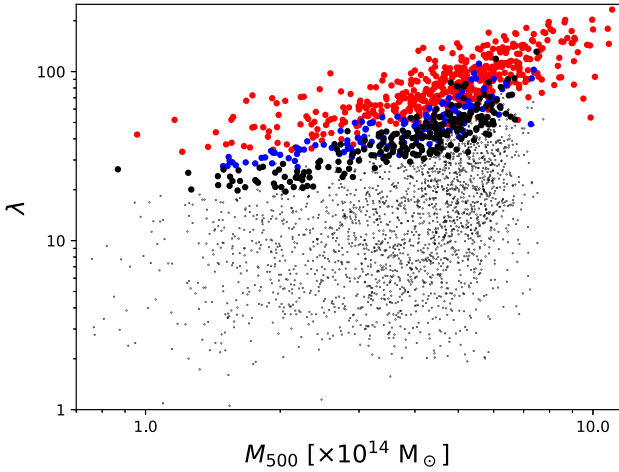
Figure E1. Richness versus mass for the *Planck* cluster candidates. Small black dots are candidates with $f_{cont} \geq 0.2$. Bigger black, blue and red points represent counterparts with $0.1 \leq f_{cont} < 0.2$, $0.05 \leq f_{cont} < 0.1$ and $f_{cont} < 0.05$, respectively.

should give an estimate of the number of real clusters within this redshift range. Finally, we will use the derived parameters from the scaling relation and we will map from λ_{MCMF} to Y_{5R500} on our excess clusters, using the $M_{500}-Y_{5R500}$ relation from equation (2). With this, we can estimate the ratio of excess candidates with $Y_{5R500} \geq Y_{5R500}^{min}$ with respect to the total number of excess candidates, which would give us an indication of how many real systems we expect to lose when applying this limiting value.

E1 Richness–mass relation

Previous analyses have shown that the number of galaxies in a cluster (or richness) is approximately linearly proportional to the cluster mass (Lin, Mohr & Stanford 2004; Gladders et al. 2007; Rozo et al. 2009a, b; Klein et al. 2019), with some intrinsic scatter ($\sigma_{int} \approx 25$ per cent; Rozo & Rykoff 2014). Fig. E1 shows how the derived masses behave with the estimated MCMF richness of the candidates. Colours red, blue, and black represent the different f_{cont} selection thresholds following Fig. 6. Although at $f_{cont} > 0.2$ the cloud of points does not seem follow any particular relation, the more reliable clusters with $f_{cont} < 0.2$ exhibit a roughly linear trend at $M_{500} \gtrsim 2.5 \times 10^{14}$ M$_\odot$. The trend is stronger at lower f_{cont}, where the contamination of the cluster sample is lowest.

We fit a $\lambda_{MCMF}-M_{500}$ relation to our data but only for the high S/N sample (S/N>4.5 and $f_{cont}^{max} = 0.3$), which, assuming a catalogue contamination of $f_{SZE-cont} \approx 8.5$ per cent (Section 2.2), means a purity of ~97.4 per cent. For the fitting, we follow a similar procedure as the one described in Klein et al. (2022), where the distribution of richnesses λ_{MCMF} is assumed to follow a log-normal distribution which depends on the mass M_{500} and redshift z, so that

$$P(\ln\lambda|M_{500}, z) = \mathcal{N}(\ln\lambda; \langle\ln\lambda\rangle(M_{500}, z), \sigma^2(M_{500}, z)), \quad \text{(E1)}$$

with mean

$$\langle\ln\lambda\rangle(M_{500}, z) = \ln\lambda_0 + \alpha_0 + \alpha_M \ln\left(\frac{M_{500}}{M_0}\right) + \alpha_z \ln\left(\frac{1+z}{1+z_0}\right) \quad \text{(E2)}$$

and variance

$$\sigma^2(M_{500}, z) = \exp(\ln\zeta(z) - \langle\ln\lambda\rangle) + \exp(s), \quad \text{(E3)}$$

where λ_0, M_0, and z_0 are pivots and (α_0, α_M, α_z, and s) are constrained by the likelihood analysis. For the pivots we use the median values of the richness, mass and redshift of the S/N>4.5 sample. The $\zeta(z)$ parameter corresponds to the richness correction factor used on MCMF (see equation 7 from Klein et al. 2019). This first term on the variance captures the Poisson noise on the measured richness, while the second term represents the intrinsic variance within the cluster population. We refer the reader to appendix A of Klein et al. (2022) for further details on the likelihood analysis. We find best-fitting values for the parameters of $\alpha_0 = -0.004 \pm 0.023$, $\alpha_M = 0.961 \pm 0.071$, $\alpha_z = 0.095 \pm 0.252$, and $s = -2.151 \pm 0.101$.

E2 On the difference between 51 per cent and 75 per cent initial contamination

For the distribution of excess candidates, we use the PSZ-MCMF cluster catalogue to define the redshift ranges using the 25 per cent, 50 per cent, and 75 per cent percentiles, corresponding to ranges of $0 < z \leq 0.18$, $0.18 < z \leq 0.29$, $0.29 < z \leq 0.44$, and $0.44 < z \leq 1.32$. For each of these ranges we look at the λ_{MCMF} distribution of *Planck* candidates and that of the random lines of sight, rescaling the latter to fit the candidates distribution at low λ_{MCMF}. We then subtract the number of scaled random lines of sight to the number of *Planck* candidates for each λ_{MCMF} bin within a redshift range. We refer to this as the distribution of excess candidates, which maps the distribution of real clusters down to low λ without accounting for catalogue purity, unlike when a f_{cont} threshold f_{cont}^{max} is applied.

Finally we transform this λ_{MCMF} distribution into a M_{500} distribution, and then into a Y_{5R500} distribution. Fig. E2 shows the different steps on the estimation of the excess and the final transformations. The top panel shows the distributions of candidates and scaled random lines of sight for the $0 < z \leq 0.18$ redshift range as purple and orange lines, respectively, with the excess candidates, labeled as 'residual', shown in red. The bottom shows the distribution of the excess candidates for the different redshift bins in terms of Y_{5R500}. The vertical grey line marks the Y_{5R500}^{min}. Depending on how we scale the randoms to fit the low richness regime of the candidates, the ratio of the total excess candidates (summed at all redshifts) to that of the total number of candidates varies between 55–65 per cent. Of those, ~50 per cent are below the Y_{5R500}^{min} threshold, regardless of the normalization, meaning that we would expect to lose half of the real sources by applying this threshold.

We note that we do not probe the $\lambda_{MCMF}-M_{500}$ relation at $\lambda < 10$ (see Fig. E1), which, depending on the redshift, could translate to $M_{500} < 10^{14}$ M$_\odot$. However, this does not affect our analysis because, as can be seen in Fig. 6, the minimum λ in our sample is $\lambda_{min} \sim 20$ at $z \approx 0.03$, which corresponds to a mass $M_{500} > 10^{14}$ M$_\odot$ using our scaling relation.

The different arrows on the bottom panel show, for each redshift range, the richness of a source with $f_{cont} = 0.2$, $\lambda_{MCMF, min}$, translated into a $Y_{5R500,min}$, colour coded according to the redshift range. Each $\lambda_{MCMF, min}(z)$ is estimated using the median redshift of each redshift range. These arrows can be interpreted as the selection thresholds that are applied when selecting candidates with $f_{cont} < 0.2$, showing good agreement with Y_{5R500}^{min} at all redshifts. This can also be seen in Fig. 9, where at $f_{cont}^{max} = 0.2$, the number of clusters over the number of candidates is ~25 per cent, similar to the value expected using Y_{5R500}^{min} (Section 2.2).

We note that groups and clusters corresponding to the difference between 51 per cent and 75 per cent have $0.2 < f_{cont} < 0.65$. They correspond to small black dots in Fig. E1 and are thus subject to a strong selection bias. For these systems, the measured SZE signal is
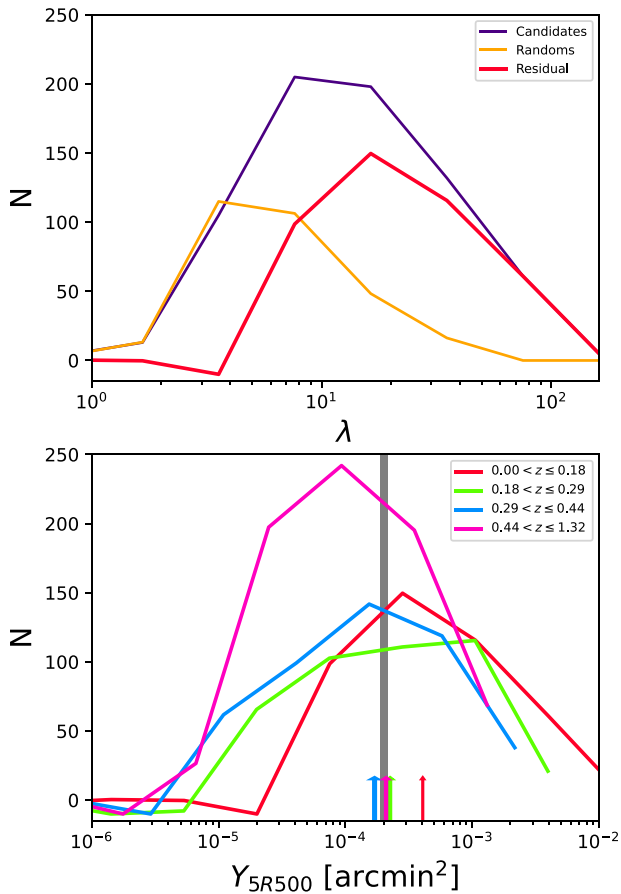
Figure E2. *Top:* Richness distributions in the redshift range $0 < z_{\mathrm{MCMF}} \leq 0.18$ of candidates, rescaled randoms, and excess candidates shown as purple, orange, and red lines, respectively. *Bottom:* Y_{5R500} distributions of excess candidates for different redshift bins. Y_{5R500} is determined from λ_{MCMF} using scaling relations. Coloured arrows correspond to the richness derived Y_{5R500} a candidate would need to have for us to consider it a real cluster in our sample, estimated using the median redshift of all the candidates for each redshift bin. The grey line marks the $Y_{5R500}^{\min}$ used to estimate the purity in Section 2.2.

dominated by a positive noise fluctuation on top of an actual small SZ signal from the cluster. The conversion of the measured SZE signal to the mass thus provides strongly overestimated values. However, we are already excluding most of these systems in the final catalogue where we only add 11 S/N>4.5 clusters with $0.2 \leq f_{\mathrm{cont}} < 0.3$.

[1]*Faculty of Physics, Ludwig-Maximilians-Universität, Scheinerstr. 1, D-81679 Munich, Germany*
[2]*Excellence Cluster Origins, Boltzmannstr. 2, D-85748 Garching, Germany*
[3]*Max Planck Institute for Extraterrestrial Physics, Giessenbachstrasse, D-85748 Garching, Germany*
[4]*IRFU, CEA, Université Paris-Saclay, F-91191 Gif-sur-Yvette, France*
[5]*AIM, CEA, CNRS, Université Paris-Saclay, Université Paris Diderot, Sorbonne Paris Cité, F-91191 Gif-sur-Yvette, France*
[6]*Observatorio Astronómico Nacional (OAN-IGN), C/ Alfonso XII 3, E-28014 Madrid, Spain*
[7]*Cerro Tololo Inter-American Observatory, NSF's National Optical-Infrared Astronomy Research Laboratory, Casilla 603, La Serena, Chile*
[8]*Laboratório Interinstitucional de e-Astronomia - LIneA, Rua Gal. José Cristino 77, Rio de Janeiro, RJ - 20921-400, Brazil*
[9]*Department of Physics, University of Michigan, Ann Arbor, MI 48109, USA*
[10]*Institute of Cosmology and Gravitation, University of Portsmouth, Portsmouth, PO1 3FX, UK*
[11]*CNRS, UMR 7095, Institut d'Astrophysique de Paris, F-75014 Paris, France*
[12]*Sorbonne Universités, UPMC Univ Paris 06, UMR 7095, Institut d'Astrophysique de Paris, F-75014 Paris, France*
[13]*Department of Physics & Astronomy, University College London, Gower Street, London, WC1E 6BT, UK*
[14]*Kavli Institute for Particle Astrophysics & Cosmology, PO Box 2450, Stanford University, Stanford, CA 94305, USA*
[15]*SLAC National Accelerator Laboratory, Menlo Park, CA 94025, USA*
[16]*Instituto de Astrofisica de Canarias, E-38205 La Laguna, Tenerife, Spain*
[17]*Universidad de La Laguna, Dpto. Astrofísica, E-38206 La Laguna, Tenerife, Spain*
[18]*Center for Astrophysical Surveys, National Center for Supercomputing Applications, 1205 West Clark St., Urbana, IL 61801, USA*
[19]*Department of Astronomy, University of Illinois at Urbana-Champaign, 1002 W. Green Street, Urbana, IL 61801, USA*
[20]*Institut de Física d'Altes Energies (IFAE), The Barcelona Institute of Science and Technology, Campus UAB, E-08193 Bellaterra (Barcelona), Spain*
[21]*Institut d'Estudis Espacials de Catalunya (IEEC), E-08034 Barcelona, Spain*
[22]*Institute of Space Sciences (ICE, CSIC), Campus UAB, Carrer de Can Magrans, s/n, E-08193 Barcelona, Spain*
[23]*Astronomy Unit, Department of Physics, University of Trieste, via Tiepolo 11, I-34131 Trieste, Italy*
[24]*INAF − Osservatorio Astronomico di Trieste, via G. B. Tiepolo 11, I-34143 Trieste, Italy*
[25]*Institute for Fundamental Physics of the Universe, Via Beirut 2, I-34014 Trieste, Italy*
[26]*Hamburger Sternwarte, Universität Hamburg, Gojenbergsweg 112, D-21029 Hamburg, Germany*
[27]*Department of Physics, IIT Hyderabad, Kandi, 502285 Telangana, India*
[28]*Fermi National Accelerator Laboratory, PO Box 500, Batavia, IL 60510, USA*
[29]*Jet Propulsion Laboratory, California Institute of Technology, 4800 Oak Grove Dr., Pasadena, CA 91109, USA*
[30]*Institute of Theoretical Astrophysics, University of Oslo. PO Box 1029 Blindern, NO-0315 Oslo, Norway*
[31]*Kavli Institute for Cosmological Physics, University of Chicago, Chicago, IL 60637, USA*
[32]*Instituto de Fisica Teorica UAM/CSIC, Universidad Autonoma de Madrid, E-28049 Madrid, Spain*
[33]*Observatório Nacional, Rua Gal. José Cristino 77, Rio de Janeiro, RJ-20921-400, Brazil*
[34]*School of Mathematics and Physics, University of Queensland, Brisbane, QLD 4072, Australia*
[35]*Santa Cruz Institute for Particle Physics, Santa Cruz, CA 95064, USA*
[36]*Center for Cosmology and Astro-Particle Physics, The Ohio State University, Columbus, OH 43210, USA*
[37]*Department of Physics, The Ohio State University, Columbus, OH 43210, USA*
[38]*Center for Astrophysics | Harvard & Smithsonian, 60 Garden Street, Cambridge, MA 02138, USA*
[39]*Australian Astronomical Optics, Macquarie University, North Ryde, NSW 2113, Australia*
[40]*Lowell Observatory, 1400 Mars Hill Rd, Flagstaff, AZ 86001, USA*
[41]*Centre for Gravitational Astrophysics, College of Science, The Australian National University, ACT 2601, Australia*
[42]*The Research School of Astronomy and Astrophysics, Australian National University, ACT 2601, Australia*
[43]*Department of Astrophysical Sciences, Princeton University, Peyton Hall, Princeton, NJ 08544, USA*
[44]*Centro de Investigaciones Energéticas, Medioambientales y Tecnológicas (CIEMAT), Madrid, Spain*
[45]*Institució Catalana de Recerca i Estudis Avançats, E-08010 Barcelona, Spain*

[46]*Department of Astronomy, University of California, Berkeley, 501 Campbell Hall, Berkeley, CA 94720, USA*

[47]*Institute of Astronomy, University of Cambridge, Madingley Road, Cambridge CB3 0HA, UK*

[48]*Department of Physics and Astronomy, University of Pennsylvania, Philadelphia, PA 19104, USA*

[49]*Department of Physics and Astronomy, Pevensey Building, University of Sussex, Brighton, BN1 9QH, UK*

[50]*School of Physics and Astronomy, University of Southampton, Southampton, SO17 1BJ, UK*

[51]*Computer Science and Mathematics Division, Oak Ridge National Laboratory, Oak Ridge, TN 37831, USA*

[52]*Lawrence Berkeley National Laboratory, 1 Cyclotron Road, Berkeley, CA 94720, USA*

This paper has been typeset from a TEX/LATEX file prepared by the author.